TOPICAL REVIEW • OPEN ACCESS

Topological surface states in nodal superconductors

To cite this article: Andreas P Schnyder and Philip M R Brydon 2015 *J. Phys.: Condens. Matter* **27** 243201

OPEN ACCESS
IOP Publishing
Journal of Physics: Condensed Matter
J. Phys.: Condens. Matter **27** (2015) 243201 (20pp)
doi:10.1088/0953-8984/27/24/243201

Topical Review

Topological surface states in nodal superconductors

Andreas P Schnyder[1] **and Philip M R Brydon**[2]

[1] Max-Planck-Institut für Festkörperforschung, Heißenbergstrasse 1, D-70569 Stuttgart, Germany
[2] Condensed Matter Theory Center and Joint Quantum Institute, University of Maryland, College Park, MD 20742, USA

E-mail: a.schnyder@fkf.mpg.de and pbrydon@umd.edu

Received 12 February 2015, revised 27 March 2015
Accepted for publication 1 April 2015
Published 22 May 2015

Abstract

Topological superconductors have become a subject of intense research due to their potential use for technical applications in device fabrication and quantum information. Besides fully gapped superconductors, unconventional superconductors with point or line nodes in their order parameter can also exhibit nontrivial topological characteristics. This article reviews recent progress in the theoretical understanding of nodal topological superconductors, with a focus on Weyl and noncentrosymmetric superconductors and their protected surface states. Using selected examples, we review the bulk topological properties of these systems, study different types of topological surface states, and examine their unusual properties. Furthermore, we survey some candidate materials for topological superconductivity and discuss different experimental signatures of topological surface states.

Keywords: unconventional superconductor, topology, surface states, Berry phase, tunelling phenomena

(Some figures may appear in colour only in the online journal)

1. Introduction

The discovery that gapped electronic systems can possess nontrivial topology has sparked a revolution in condensed matter physics [1–8]. Such topological systems are characterized by a $\mathbb{Z}$ or $\mathbb{Z}_2$ topological number, and display topologically protected surface states due to the so-called bulk-boundary correspondence. Two types of such systems can be discerned: topological insulators and superconductors. While there are now many examples of topological insulators, topological superconductors have proved to be much rarer. This is due to the unconventional pairing symmetries required for a topological state. In contrast to the familiar s-wave spin-singlet pairing in conventional superconductors, such pairing states appear to require a particular constellation of pairing interactions and electronic structure, and are not robust to disorder. Topological superconductors are nevertheless of great interest due to the existence of protected Majorana surface states, which arise as a consequence of a nontrivial topology of the bulk quasiparticle wavefunctions. These surface states may have important applications in quantum information technology, and have motivated an intense effort to 'engineer' a topological superconducting state from more prosaic components [9–12]. While there are many such proposals, at present the most promising is to proximity-induce p-wave superconductivity in a semiconductor with strong spin-orbit coupling (SOC) [13–17].

Although superconductors with unconventional pairing symmetries are not uncommon, they rather typically display points or lines on the Fermi surface where the superconducting gap vanishes, so-called 'nodes'. As such, they are not covered by the 'ten fold way' classification of the topology

of *fully gapped* electronic systems [1–4]. Nevertheless, such systems can display interesting topological properties, and possess topologically protected edge states, although the protection is weaker than for fully gapped systems [18–32]. Although global topological invariants cannot be defined for gapless systems, it is nevertheless possible to classify the rich topological structure of nodal superconductors in terms of momentum dependent topological numbers. This has revealed that many nodal topological superconductors and superfluids have nontrivial topology, e.g. the high-T_c $d_{x^2-y^2}$-wave superconductors [33–36], the heavy Fermion systems $CeCoIn_5$ [37–40] and URu_2Si_2 [41–44], nodal noncentrosymmetric superconductors [20–24, 45, 46], Weyl superconductors [47–50], oxide interfaces [51], and the A phase of superfluid ^{3}He [25–28, 52]. Similar to fully gapped topological superconductors, the topological characteristics of nodal superconducting states reveal themselves at the surface in the form of Majorana cone states, Majorana flat-band states, or arc surface states [22].

Our aim in this review is to provide a thorough introduction to the field of nodal topological superconductors, acting as a manual and reference for both theorists and experimentalists. We do not wish to deliver an exhaustive overview of all nodal superconductors, however, but rather to show via selected examples the different topological structures which can be realized and what type of unconventional properties these materials exhibit. While the concepts that we discuss can be generally applied to all nodal topological systems, our focus shall be upon systems where the superconductivity is an intrinsic property, as opposed to engineered nodal superconducting states in heterostructures.

We give a brief outline of the review here. We commence in section 2 by introducing our two model systems: Weyl superconductors and noncentrosymmetric superconductors, which are prototypes for topological superconductors with point and line nodes, respectively. In section 3 we set out the topological classification of the nodal states in terms of a 'periodic table' of the nodal structure, and apply this to our canonical examples. The topologically protected surface states are studied in section 4 using a quasiclassical method, which forms a useful basis for understanding the experimental signatures of the topological surface states in section 5. We survey candidate nodal topological superconductors in section 6, before concluding with a brief outlook for the field.

2. Phenomenological models

While there are a plethora of nodal superconductors with nontrivial topology, it is convenient to illustrate our discussion with straightforward but physically relevant phenomenological models. Here we introduce three such systems: the p-wave Weyl superconductor, the d-wave Weyl superconductor, and noncentrosymmetric superconductors. Our choice is motivated by a desire to exemplify line and point nodal structures, and we therefore take the simplest normal-state electronic Hamiltonian consistent with the symmetries. Although for realistic systems one must often consider more complicated models, e.g. including multiorbital effects, these nonuniversal considerations obscure the topological properties of the gap functions. We shall return to these model systems throughout the review.

2.1. Topological superconductors with point nodes

We consider two different phenomenological models of superconductors/superfluids with point nodes. The first one is the Anderson-Brinkman-Morel (ABM) state [52–54], which is believed to occur in the A phase of superfluid ^{3}He as well as in cold atomic and polar molecular gases [55]. The ABM state is a three-dimensional superfluid of spinless (or fully spin-polarized) fermions with $(p_x \pm \mathrm{i}p_y)$-wave pairing and is described by the Bogoliubov-de Gennes (BdG) Hamiltonian $\mathcal{H} = \frac{1}{2}\sum_{\mathbf{k}} \phi_{\mathbf{k}}^\dagger \mathcal{H}(\mathbf{k})\phi_{\mathbf{k}}$ with

$$\mathcal{H}(\mathbf{k}) = h(\mathbf{k})\tau_z + \frac{\Delta_0}{k_\mathrm{F}}\mathbf{k}\cdot\left(\hat{\mathbf{e}}_1\tau_x + \hat{\mathbf{e}}_2\tau_y\right), \tag{1}$$

where $\phi_{\mathbf{k}} = (c_{\mathbf{k}}, c_{\mathbf{k}}^\dagger)^\mathrm{T}$ and $c_{\mathbf{k}}^\dagger(c_{\mathbf{k}})$ is the creation (annihilation) operator of spinless fermions with momentum $\mathbf{k}$. Here, τ_i denotes the three Pauli matrices which act in particle–hole space, $h(\mathbf{k})$ is the normal-state dispersion, k_F is the Fermi wave vector, and Δ_0 denotes the amplitude of the superconducting order parameter. The direction of the orbital momentum of the Cooper pair is defined by $\hat{\mathbf{l}} = \hat{\mathbf{e}}_1 \times \hat{\mathbf{e}}_2$. In the following we assume a spherical Fermi surface centered at the Γ point and a momentum independent vector $\hat{\mathbf{l}}$ pointing along the k_z axis in the Brillouin zone. Thus, the eigenvalues of Hamiltonian (1) are $\pm\lambda(\mathbf{k}) = \pm\sqrt{[h(\mathbf{k})]^2 + (\Delta_0/k_\mathrm{F})^2(k_x^2 + k_y^2)}$, and the spectrum $\lambda(\mathbf{k})$ exhibits two Weyl nodes at the north and south poles of the Fermi sphere $\mathbf{K}_\pm = (0, 0, \pm k_\mathrm{F})$. The low-energy physics in the vicinity of the point nodes $\mathbf{K}_\pm$ can be captured by the anisotropic Weyl Hamiltonian

$$\mathcal{H}_\pm(\mathbf{p}) = (\Delta_0/k_\mathrm{F})(p_x\tau_x + p_y\tau_y) \pm \hbar v_\mathrm{F} p_z \tau_z, \tag{2}$$

where $\mathbf{p} = \mathbf{k} - \mathbf{K}_\pm$ and $v_\mathrm{F} = \hbar k_\mathrm{F}/m$ denotes the Fermi velocity. Hence, equation (1) defines the simplest version of a Weyl superconductor with two point nodes. We note that, in contrast to ordinary point nodes, the bands crossing at a Weyl node are individually nondegenerate. Moreover, Weyl nodes are impossible to gap out, since there exists no 'fourth Pauli matrix' that anticommutes with the three Pauli matrices τ_i of equation (2). The dispersion close to the Weyl points is linear in all three directions, leading to a density of states that increases quadratically with energy. As opposed to Weyl points in semimetals, the particle-hole symmetry dictates that the point nodes $\mathbf{K}_\pm$ remain pinned at zero energy even as the chemical potential is varied. Each Weyl node can be characterized in terms of a chirality index, which measures the relative handedness of the three momenta $\mathbf{p}$ with respect to the Pauli matrices in equation (2). For Hamiltonian $\mathcal{H}_\pm(\mathbf{p})$ the chirality of the Weyl point is ± 1. We note that while arbitrary (small) perturbations of Hamiltonian (2) in general lead to a shift of the point nodes, they cannot open up a gap in the spectrum. We will see in section 3.3.1 that the stability of the Weyl nodes is protected by a Chern number (or Skyrmion number), which takes on the values ± 1.

As a second example of a superconductor with point nodes, we consider the three-dimensional spin-singlet chiral $(d_{x^2-y^2} \pm \mathrm{i}d_{xy})$-wave state, which is likely realized in the heavy fermion system URu_2Si_2 [41–44] and the pnictide material SrPtAs [47, 48]. The BdG Hamiltonian of this chiral superconducting phase is given by $\mathcal{H} = \frac{1}{2}\sum_{\mathbf{k}} \Phi_{\mathbf{k}}^{\dagger}\mathcal{H}(\mathbf{k})\Phi_{\mathbf{k}}$, with

$$\mathcal{H}(\mathbf{k}) = h(\mathbf{k})\tau_z + \frac{\Delta_0}{k_{\mathrm{F}}^2}\left[(k_x^2 - k_y^2)\tau_x + 2k_x k_y \tau_y\right] \tag{3}$$

and the Nambu spinor $\Phi_{\mathbf{k}} = (c_{\mathbf{k}\uparrow}, c_{-\mathbf{k}\downarrow}^{\dagger})^{\mathrm{T}}$, where $c_{\mathbf{k}\sigma}^{\dagger}(c_{\mathbf{k}\sigma})$ represents the electron creation (annihilation) operator with momentum $\mathbf{k}$ and spin σ. Observe that for this pairing symmetry the orbital angular momentum projected along the k_z axis is ± 2, whereas for the $(p_x \pm \mathrm{i}p_y)$-wave state discussed above it is ± 1. Similar to equation (1), we find that for a spherical Fermi surface centered at the Γ point, Hamiltonian (3) exhibits two point nodes located at $\mathbf{K}_{\pm} = (0, 0, \pm k_{\mathrm{F}})$, which are double Weyl points pinned at zero energy by the particle-hole symmetry. Expanding equation (3) around $\mathbf{K}_{\pm}$ to second order in the momentum, we obtain the following low-energy description of the double Weyl nodes

$$\mathcal{H}_{\pm}(\mathbf{p}) = \frac{\Delta_0}{k_{\mathrm{F}}^2}\left[(p_x^2 - p_y^2)\tau_x + 2p_x p_y \tau_y\right] + \left[\frac{\hbar^2}{2m}|\mathbf{p}|^2 \pm \hbar v_{\mathrm{F}} p_z\right]\tau_z, \tag{4}$$

where $\mathbf{p} = \mathbf{k} - \mathbf{K}_{\pm}$. Hence, the low-energy nodal quasiparticles near $\mathbf{K}_{\pm}$ exhibit linear and quadratic dispersions along the p_z direction and in the $p_x p_y$ plane, respectively. All in all, this anisotropic dispersion leads to a density of states which increases linearly with energy. As explained in section 3.3.2, the double Weyl points (4) are protected against gap opening by the conservation of a Chern or Skyrmion number that takes on the values ± 2.

2.2. Topological superconductors with line nodes

The prototype of a topological superconductor with line nodes are time-reversal-symmetric three-dimensional noncentrosymmetric superconductors (NCS). In these systems, the crystal structure breaks inversion symmetry leading to strong electric field gradients within the unit cell, which in turn generates strong SOC. Furthermore, the absence of inversion symmetry means that parity is no longer a good quantum number, and so a mixed pairing state with both singlet and triplet gaps is possible.

The minimal description for such a system has the BdG Hamiltonian $\mathcal{H} = \frac{1}{2}\sum_{\mathbf{k}} \psi_{\mathbf{k}}^{\dagger}\mathcal{H}(\mathbf{k})\psi_{\mathbf{k}}$, with

$$\mathcal{H}(\mathbf{k}) = \begin{pmatrix} h(\mathbf{k}) & \Delta(\mathbf{k}) \\ \Delta^{\dagger}(\mathbf{k}) & -h^{T}(-\mathbf{k}) \end{pmatrix} \tag{5}$$

and $\psi_{\mathbf{k}} = (c_{\mathbf{k}\uparrow}, c_{\mathbf{k}\downarrow}, c_{-\mathbf{k}\uparrow}^{\dagger}, c_{-\mathbf{k}\downarrow}^{\dagger})^{\mathrm{T}}$, where $c_{\mathbf{k}\sigma}^{\dagger}$ $(c_{\mathbf{k}\sigma})$ denotes the electron creation (annihilation) operator with momentum $\mathbf{k}$ and spin σ. The normal-state dispersion of the electrons in the spin basis is given by

$$h(\mathbf{k}) = \varepsilon_{\mathbf{k}}\sigma_0 + \mathbf{g}_{\mathbf{k}} \cdot \boldsymbol{\sigma}, \tag{6}$$

where $\varepsilon_{\mathbf{k}}$ is the nonmagnetic dispersion while $\mathbf{g}_{\mathbf{k}}$ denotes the SOC potential. $\boldsymbol{\sigma} = (\sigma_x, \sigma_y, \sigma_z)$ denotes the vector of the Pauli matrices, while σ_0 stands for the 2×2 unit matrix. By time-reversal symmetry, we require that $\varepsilon_{\mathbf{k}}$ and $\mathbf{g}_{\mathbf{k}}$ are symmetric and antisymmetric in $\mathbf{k}$, respectively. The normal-state Hamiltonian (6) is diagonalized in the so-called helicity basis, taking the form $\tilde{h}(\mathbf{k}) = \mathrm{diag}(\xi_{\mathbf{k}}^{+}, \xi_{\mathbf{k}}^{-})$, where $\xi_{\mathbf{k}}^{\pm} = \varepsilon_{\mathbf{k}} \pm |\mathbf{g}_{\mathbf{k}}|$ is the dispersion of the positive-helicity and negative-helicity bands, respectively.

The superconducting gap contains both even-parity spin-singlet and odd-parity spin-triplet pairing potentials

$$\Delta(\mathbf{k}) = (\psi_{\mathbf{k}}\sigma_0 + \mathbf{d}_{\mathbf{k}} \cdot \boldsymbol{\sigma})\left(\mathrm{i}\sigma_y\right), \tag{7}$$

where $\psi_{\mathbf{k}}$ and $\mathbf{d}_{\mathbf{k}}$ represent the spin-singlet and spin-triplet components, respectively. In a time-reversal-symmetric system they have the same global phase, and without loss of generality we assume them to be real. It is well known that in the absence of interband pairing, the superconducting transition temperature is maximized when the spin-triplet pairing vector $\mathbf{d}_{\mathbf{k}}$ is aligned with the polarization vector $\mathbf{g}_{\mathbf{k}}$ of the SOC [56]. This implies that there is only pairing between states on the same helicity Fermi surface, with positive and negative helicity gaps $\Delta_{\mathbf{k}}^{\pm} = \psi_{\mathbf{k}} \pm |\mathbf{d}_{\mathbf{k}}|$. Assuming an s-wave like order parameter for the singlet pairing, we observe that while the positive-helicity Fermi surface is fully gapped, the negative-helicity gap may possess nodes. We parametrize the singlet and triplet components of the superconducting gap function as

$$\psi_{\mathbf{k}} = \Delta_s = r\,\Delta_0, \tag{8}$$

$$\mathbf{d}_{\mathbf{k}} = \Delta_t \mathbf{l}_{\mathbf{k}} = (1 - r)\,\Delta_0 \mathbf{l}_{\mathbf{k}}, \tag{9}$$

where $\mathbf{l}_{\mathbf{k}} = \mathbf{g}_{\mathbf{k}}/\lambda$, with λ the SOC strength. Here, r parametrizes the mixed pairing state, tuning the system between purely triplet $(r = 0)$ and purely singlet $(r = 1)$ gaps.

3. Topological classification of nodal superconductors

The topological properties of nodal superconductors (and semimetals) can be classified in a similar manner as those of fully gapped superconductors (and insulators) [1–3]. A nodal point or nodal line in a superconductor is topologically stable if there does not exist any symmetry preserving mass term that opens up a full gap in the spectrum. The topological stability of these point or line nodes is guaranteed by the conservation of a topological charge (i.e. a topological invariant), which is defined in terms of an integral along a contour that encloses (encircles) the point node (line node). These topological invariants can be either Chern or winding numbers, referred to as '$\mathbb{Z}$ invariants' (or '$2\mathbb{Z}$ invariants'), or binary invariants, referred to as '$\mathbb{Z}_2$ numbers'. In this section we briefly review the ten-fold classification of nodal topological superconductors (and semimetals) [57–61]. This scheme classifies point and line nodes in nodal superconductors (Fermi points and Fermi lines in semimetals) in terms of global symmetries, i.e. nonspatial symmetries that act locally in position space, namely, time-reversal symmetry (TRS), particle-hole symmetry (PHS), and chiral or sublattice symmetry (SLS).

Table 1. Ten-fold classification of nodal points/lines and Fermi surfaces in superconductors and semimetals, respectively [57–59, 61]. The first and second rows indicate the codimension $p = d_{\mathrm{BZ}} - d_{\mathrm{n}}$ of the nodal lines at high-symmetry points and away from high-symmetry points of the Brillouin zone, respectively. The first column lists the ten symmetry classes (using the 'Cartan nomenclature' [3]), which are distinguished by the presence or absence of TRS (T), PHS (C), and chiral symmetry (S). The second and third columns indicate the sign of the squared symmetry operators T^2 and C^2, respectively. The absence of symmetries is denoted by '0'. The presence of chiral symmetry S is denoted by '1'.

At high-sym. point Off high-sym. point	T	C	S	$p=8$ $p=2$	$p=1$ $p=3$	$p=2$ $p=4$	$p=3$ $p=5$	$p=4$ $p=6$	$p=5$ $p=7$	$p=6$ $p=8$	$p=7$ $p=1$
A	0	0	0	0	$\mathbb{Z}$	0	$\mathbb{Z}$	0	$\mathbb{Z}$	0	$\mathbb{Z}$
AIII	0	0	1	$\mathbb{Z}$	0	$\mathbb{Z}$	0	$\mathbb{Z}$	0	$\mathbb{Z}$	0
AI	+1	0	0	0	0	0	$2\mathbb{Z}$	0	$\mathbb{Z}_2$[a,b]	$\mathbb{Z}_2$[a,b]	$\mathbb{Z}$
BDI	+1	+1	1	$\mathbb{Z}$	0	0	0	$2\mathbb{Z}$	0	$\mathbb{Z}_2$[a,b]	$\mathbb{Z}_2$[a,b]
D	0	+1	0	$\mathbb{Z}_2$[a,b]	$\mathbb{Z}$	0	0	0	$2\mathbb{Z}$	0	$\mathbb{Z}_2$[a,b]
DIII	−1	+1	1	$\mathbb{Z}_2$[a,b]	$\mathbb{Z}_2$[a,b]	$\mathbb{Z}$	0	0	0	$2\mathbb{Z}$	0
AII	−1	0	0	0	$\mathbb{Z}_2$[a,b]	$\mathbb{Z}_2$[a,b]	$\mathbb{Z}$	0	0	0	$2\mathbb{Z}$
CII	−1	−1	1	$2\mathbb{Z}$	0	$\mathbb{Z}_2$[a,b]	$\mathbb{Z}_2$[a,b]	$\mathbb{Z}$	0	0	0
C	0	−1	0	0	$2\mathbb{Z}$	0	$\mathbb{Z}_2$[a,b]	$\mathbb{Z}_2$[a,b]	$\mathbb{Z}$	0	0
CI	+1	−1	1	0	0	$2\mathbb{Z}$	0	$\mathbb{Z}_2$[a,b]	$\mathbb{Z}_2$[a,b]	$\mathbb{Z}$	0

[a] $\mathbb{Z}_2$ numbers only protect nodal lines of dimension zero ($d_{\mathrm{n}} = 0$) at high-symmetry points of the Brillouin zone.
[b] Nodal lines of any dimension d_{n} located away from high symmetry points of the Brillouin zone cannot be protected by a $\mathbb{Z}_2$ number. However, the $\mathbb{Z}_2$ topological invariant can lead to the appearance of protected zero-energy surface states at time-reversal invariant momenta of the surface Brillouin zone.

In momentum space, TRS and PHS act on the BdG (or Bloch) Hamiltonian $\mathcal{H}(\mathbf{k})$ as

$$T^{-1}\mathcal{H}(-\mathbf{k})T = +\mathcal{H}(\mathbf{k}) \quad \text{and} \quad C^{-1}\mathcal{H}(-\mathbf{k})C = -\mathcal{H}(\mathbf{k}), \tag{10}$$

respectively, where $T = \mathcal{K}U_T$ and $C = \mathcal{K}U_C$ are antiunitary operators and $\mathcal{K}$ denotes the complex conjugation operator. Chiral symmetry, however, is implemented in terms of an anticommutation relation

$$S^{-1}\mathcal{H}(\mathbf{k})S = -\mathcal{H}(\mathbf{k}), \tag{11}$$

where S is a unitary operator. Chiral symmetry S can be viewed as a combination of time-reversal and particle-hole symmetry, i.e. $S \propto TC$. There are three different possibilities for how a given BdG (or Bloch) Hamiltonian $\mathcal{H}(\mathbf{k})$ can transform under TRS (or PHS): (i) $\mathcal{H}(\mathbf{k})$ is not symmetric under TRS (or PHS), which is denoted by '0' in table 1; (ii) $\mathcal{H}(\mathbf{k})$ is invariant under TRS (or PHS) and T (or C) squares to +1, which is denoted by '+1' in table 1; and (iii) $\mathcal{H}(\mathbf{k})$ is symmetric under TRS (or PHS) and T (or C) squares to -1, which is denoted by '-1' in table 1. Hence, there are $3 \times 3 = 9$ possibilities for how a Hamiltonian can transform under both TRS and PHS. For eight of these cases, the presence or absence of SLS is fully determined by how $\mathcal{H}(\mathbf{k})$ transforms under TRS and PHS. However, when both time-reversal and particle-hole symmetry are absent, there exists the extra possibility that the combined symmetry $S \propto TC$ is still present. Hence, altogether there are ten cases that fully exhaust all the possible transformation properties of a given Hamiltonian $\mathcal{H}(\mathbf{k})$ under global symmetries. These ten cases, each of which defines a symmetry class, are listed in the first column of table 1. We note that these ten symmetry classes are closely related to the ten classes of random matrices introduced by Altland and Zirnbauer [62, 63].

Now, the ten-fold classification of nodal superconductors (and semimetals) does not only depend on the symmetry properties of $\mathcal{H}(\mathbf{k})$ but also on the codimension

$$p = d_{\mathrm{BZ}} - d_{\mathrm{n}} \tag{12}$$

of the nodal structure, i.e. on the difference between the dimension d_{BZ} of the Brillouin zone and the dimension d_{n} of the superconducting node. Furthermore, it depends on how the superconducting nodes transform under the nonspatial symmetries [57, 61]. Two different situations have to be distinguished: (i) Each point node or line node is left invariant by nonspatial symmetries and (ii) different point nodes or line nodes are pairwise related to each other by global symmetry operations. In case (i) the superconducting nodes are located at high-symmetry points of the Brillouin zone, i.e. at time-reversal invariant momenta, whereas in case (ii) the point or line nodes are positioned away from high-symmetry points of the Brillouin zone.

3.1. Nodes at high-symmetry points

Let us start by discussing the ten-fold classification of superconducting nodes located at high symmetry points of the Brillouin zone [57–61]. For this case the classification of point nodes can be derived in a heuristic manner from the ten-fold classification of fully gapped superconductors through a dimensional reduction procedure [57]. That is, the surface state of a fully gapped d_{BZ}-dimensional topological superconductor realizes a topologically stable point node in $d_{\mathrm{BZ}} - 1$ dimensions. Indeed, the bulk topological invariant of the d_{BZ}-dimensional fully gapped superconductor is directly related to the topological charge of the nodal point at the boundary [60, 64]. From these observations it follows that the classification of global-symmetry-invariant nodal points with $d_n = 0$ is obtained from the original ten-fold classification of fully gapped superconductors by the dimensional shift $d_{\mathrm{BZ}} \to d_{\mathrm{BZ}} - 1$. This reasoning also holds for nodal structures

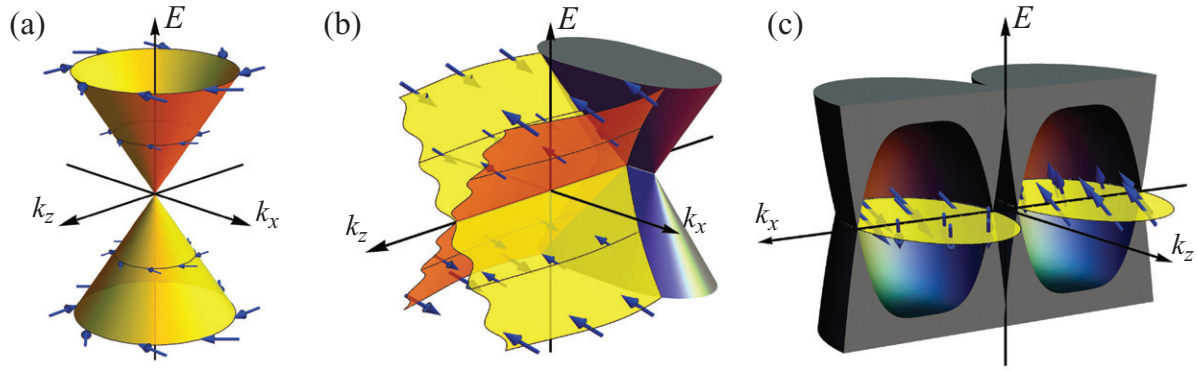

Figure 1. Energy spectrum of the three different types of topological subgap states that can exist at the surface of nodal noncentrosymmetric superconductors: (a) helical Majorana cone, (b) arc surface state, and (c) flat-band surface state. Figure adapted from [66].

with codimension $p < d_{\mathrm{BZ}}$ (i.e. $d_{\mathrm{n}} > 0$), provided that they are protected by a $\mathbb{Z}$ invariant or $2\mathbb{Z}$ invariant. $\mathbb{Z}_2$ numbers, on the other hand, guarantee only the stability of nodes with $d_{\mathrm{n}} = 0$, i.e. point nodes. These findings are confirmed by more rigorous derivations based on K theory [58–60] and minimal Dirac Hamiltonians [61]. The latter approach uses Clifford algebra to classify all possible symmetry-preserving mass terms that can be added to the Hamiltonian. The classification of global-symmetry-invariant nodal structures (and Fermi surfaces) is summarized in table 1, where the first row indicates the codimension p of the superconducting nodes. For any codimension p there are three symmetry classes for which stable superconducting nodes (or Fermi surfaces) exist that are protected by a $\mathbb{Z}$ invariant or $2\mathbb{Z}$ invariant, where the prefix '2' indicates that the topological number only takes on even values. Furthermore, in each spatial dimension d_{BZ} there exist two symmetry classes that allow for topologically stable point nodes (Fermi points) which are protected by a binary $\mathbb{Z}_2$ number.

3.2. Nodes off high-symmetry points

Second, we review the topological classification of superconductors with nodes that are located away from high-symmetry points of the Brillouin zone [57, 61]. These point or line nodes are pairwise mapped onto each other by the global antiunitary symmetries, which relate $\mathbf{k}$ to $-\mathbf{k}$. An analysis based on the minimal-Dirac-Hamiltonian method [61] shows that only $\mathbb{Z}$-type invariants can guarantee the stability of superconducting nodes off high-symmetry points, whereas $\mathbb{Z}_2$ numbers do not lead to stable nodes. However, as illustrated in terms of the example of section 3.3.3, $\mathbb{Z}_2$ numbers may nevertheless give rise to zero-energy surface states at time-reversal-invariant momenta of the surface Brillouin zone. The complete classification of superconducting nodes that are located away from high-symmetry points is presented in table 1, where the second row gives the codimension p of the superconducting node. Observe that this classification scheme is related to the ten-fold classification of fully gapped superconductors and insulators by the dimensional shift $d_{\mathrm{BZ}} \to d_{\mathrm{BZ}} + 1$.

3.3. Examples

For the phenomenological model Hamiltonians given in section 2, we derive in this subsection explicit expressions for the topological invariants that protect the superconducting nodes against gap opening. We also use these examples to illustrate the bulk-boundary correspondence [64, 65], which links the topological characteristics of the nodal gap structure to the appearance of zero-energy states at the boundary. Depending on the case, these zero-energy surface states are either linearly dispersing Majorana cones, Majorana flat bands, or arc surface states (see figure 1). We note that in real superconducting materials the gap nodes are usually positioned away from the high-symmetry points of the Brillouin zone. Indeed, this is the case for the three examples of section 2, which are therefore classified according to section 3.2. Note that the topological invariants introduced here can be straightforwardly generalized to more complicated systems.

3.3.1. The A phase of ^{3}He. The A phase of ^{3}He is phenomenologically described by Hamiltonian (1), which satisfies particle-hole symmetry $C^{-1}\mathcal{H}(-\mathbf{k})C = -\mathcal{H}(\mathbf{k})$ with $C = \mathcal{K}\tau_x$. Time-reversal symmetry, however, is broken, because the superconducting order parameter of equation (1) is complex. Hence, since $C^2 = +\mathbb{1}$, Hamiltonian (1) belongs to symmetry class D. We infer from table 1 that the Weyl nodes of the Hamiltonian (1), which have codimension $p = 3$ and occur off high symmetry points, are protected by a $\mathbb{Z}$ topological number. In order to derive a formula for this topological number it is convenient to rewrite Hamiltonian (1) as

$$\mathcal{H}(\mathbf{k}) = \mathbf{N}(\mathbf{k}) \cdot \boldsymbol{\tau}, \tag{13}$$

i.e. a dot product between the pseudospin vector $\mathbf{N}(\mathbf{k}) = \big(\Delta_0 k_x/k_{\mathrm{F}}, \Delta_0 k_y/k_{\mathrm{F}}, h(\mathbf{k})\big)$ and the vector of Pauli matrices $\boldsymbol{\tau} = (\tau_x, \tau_y, \tau_z)$. The unit vector field $\mathbf{n}_{\mathbf{k}} = \mathbf{N}(\mathbf{k})/|\mathbf{N}(\mathbf{k})|$ exhibits singular points at the Weyl nodes $\mathbf{K}_\pm$ of $\mathcal{H}(\mathbf{k})$. These point singularities realize (anti)hedgehog defects in momentum space and are characterized by the Chern number [25–28]

$$N_{\mathcal{C}} = \frac{1}{4\pi}\int_{\mathcal{C}} d^2\widetilde{\mathbf{k}}\; \mathbf{n}_{\mathbf{k}} \cdot \left[\partial_{k_1}\mathbf{n}_{\mathbf{k}} \times \partial_{k_2}\mathbf{n}_{\mathbf{k}}\right], \tag{14}$$

where $\mathcal{C}$ denotes a two-dimensional surface parametrized by $\widetilde{\mathbf{k}} = (k_1, k_2)$, which encloses one of the two Weyl nodes. Choosing $\mathcal{C}$ to be a sphere S^2 centered at one of the two Weyl points, the integral (14) can be straightforwardly evaluated. The nodes at $\mathbf{K}_\pm = (0, 0, \pm k_\mathrm{F})$ have topological charge $N_{S^2} = \pm 1$. We note that $\mathbf{n}_\mathbf{k}$ restricted to the sphere S^2 in momentum space defines a map from $\mathbf{k} \in S^2$ to the space $\mathbf{n}_\mathbf{k} \in S^2$. The Chern number N_{S^2}, equation (14), distinguishes between different homotopy classes of these maps [67]. Since the homotopy group $\pi_2(S^2)$ equals the group of the integer numbers $\mathbb{Z}$, there is an infinite number of homotopy classes of maps $\mathbf{k} \in S^2 \mapsto \mathbf{n}_\mathbf{k}$ and N_{S^2} can in general take on any integer value.

Alternatively, instead of considering a sphere S^2 one can take $\mathcal{C}$ to be a plane perpendicular to the k_z axis in the Brillouin zone. This yields $N_{k_z} = +1$ for $|k_z| < k_\mathrm{F}$ and zero otherwise. That is, the unit vector $\mathbf{n}_\mathbf{k}$ for fixed $|k_z| < k_\mathrm{F}$ possesses a unit skyrmion texture in momentum space and N_{k_z} measures its skyrmion number. In this picture, we can give the topological invariant (14) a more physical meaning by reexpressing it in terms of the Berry curvature $\mathbf{F}(\mathbf{k}) = \boldsymbol{\nabla}_\mathbf{k} \times \mathbf{A}(\mathbf{k})$, i.e.

$$N_{k_z} = \frac{1}{2\pi} \int \mathrm{d}k_x \mathrm{d}k_y \, F_z(\mathbf{k}). \tag{15}$$

Here, $\mathbf{A}(\mathbf{k}) = \mathrm{i} \langle u_-(\mathbf{k}) | \boldsymbol{\nabla}_\mathbf{k} | u_-(\mathbf{k}) \rangle$ denotes the Berry connection (also known as Berry vector potential), which is obtained from the negative-energy wavefunctions $u_-(\mathbf{k})$ of the BdG Hamiltonian. For Hamiltonian (1), the three components of the Berry curvature are given by

$$\begin{aligned} F_x(\mathbf{k}) &= \frac{\Delta_0^2 k_\mathrm{F}^2 k_x k_z}{\mu^2 \left[(k^2 - k_\mathrm{F}^2)^2 + \frac{\Delta_0^2}{\mu^2} k_\mathrm{F}^2 (k_x^2 + k_y^2) \right]^{\frac{3}{2}}}, \\ F_y(\mathbf{k}) &= \frac{\Delta_0^2 k_\mathrm{F}^2 k_y k_z}{\mu^2 \left[(k^2 - k_\mathrm{F}^2)^2 + \frac{\Delta_0^2}{\mu^2} k_\mathrm{F}^2 (k_x^2 + k_y^2) \right]^{\frac{3}{2}}}, \\ F_z(\mathbf{k}) &= \frac{\Delta_0^2 k_\mathrm{F}^2 (k_z^2 - k_x^2 - k_y^2 - k_\mathrm{F}^2)}{2\mu^2 \left[(k^2 - k_\mathrm{F}^2)^2 + \frac{\Delta_0^2}{\mu^2} k_\mathrm{F}^2 (k_x^2 + k_y^2) \right]^{\frac{3}{2}}}. \end{aligned} \tag{16}$$

The Berry curvature is plotted in figure 2(a). We observe from equation (16) that the Weyl nodes are sources and drains of Berry flux. That is, they act as unit (anti-)monopoles of the Berry curvature $\mathbf{F}(\mathbf{k})$ and there is a Berry flux of 2π flowing from one Weyl node to the other along the z direction. Along the x and y directions, on the other hand, the Berry flux is vanishing since $F_{x(y)}(\mathbf{k})$ is odd in k_x (k_y) and k_z. We also note that the Berry curvature is sharply peaked within a shell of width Δ_0 about the Fermi surface.

Due to the bulk-boundary correspondence, the band topology of Weyl superconductors gives rise to arc surface states. Consider for example Hamiltonian (1) in a three-dimensional slab geometry with a (1 0 0) surface. Because of translation invariance along the surface, the three-dimensional (1 0 0) slab can be decomposed into a family of two-dimensional (1 0) ribbons parametrized by k_z. Ribbons with a k_z in between the pair of Weyl nodes have a non-zero Chern number, i.e. $N_{k_z} = +1$ for $|k_z| < k_\mathrm{F}$, while for $|k_z| > k_\mathrm{F}$ the topology is trivial. Each ribbon with $|k_z| < k_\mathrm{F}$ can be interpreted as a two-dimensional fully gapped $(p_x + \mathrm{i}p_y)$-wave superconductor with a chiral Majorana edge mode. Hence, the Majorana surface states of the Weyl superconductor form a one-dimensional open arc in the surface Brillouin zone, connecting the projected Weyl nodes of the bulk gap. (See figure 4(a) and section 4.2). These chiral surface states give rise to anomalous spin and thermal Hall effects which are proportional to the separation of the Weyl nodes in momentum space. (see section 5.2).

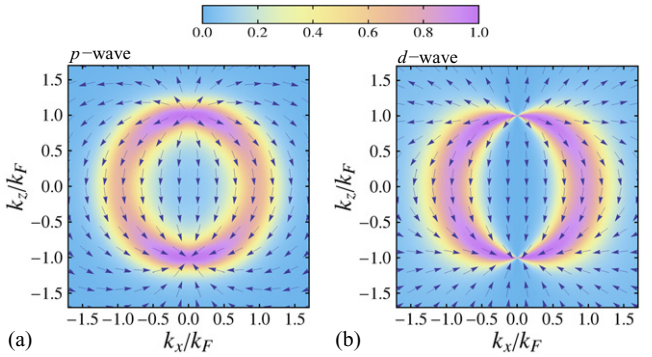

Figure 2. Berry curvature in (a) the $(p_x + \mathrm{i}p_y)$-wave and (b) the $(d_{x^2-y^2} + \mathrm{i}d_{xy})$-wave Weyl superconductor in the k_x-k_z plane. The arrows indicate the direction of $\mathbf{F}(\mathbf{k})$ while the colour scale gives $\frac{2}{\pi} \arctan(|\mathbf{F}(\mathbf{k})|)$. We choose $\Delta_0 = 0.5\mu$; realistic values of $\Delta_0 \ll \mu$ give a curvature which is much more sharply peaked at the Fermi surface.

3.3.2. Chiral $(d_{x^2-y^2} \pm \mathrm{i}d_{xy})$-wave superconductor. The spin-singlet chiral $(d_{x^2-y^2} \pm \mathrm{i}d_{xy})$-wave superconductor (3) satisfies both particle-hole symmetry and $SU(2)$ spin-rotation symmetry and therefore belongs to symmetry class C in table 1 (or alternatively to class A if one considers only a $U(1)$ part of the spin-rotation symmetry). Hence, as indicated by the classification table, the Weyl nodes of Hamiltonian (3) (which occur off high symmetry points) are protected by a $2\mathbb{Z}$ invariant, which takes on only even values. This topological number is given by the same expression as equation (14) but with $\mathbf{N}(\mathbf{k}) = \big(\Delta_0(k_x^2 - k_y^2)/k_\mathrm{F}^2, 2\Delta_0 k_x k_y / k_\mathrm{F}^2, h(\mathbf{k})\big)$. As opposed to the previous example, the unit vector $\mathbf{n}_\mathbf{k} = \mathbf{N}(\mathbf{k})/|\mathbf{N}(\mathbf{k})|$ for fixed $|k_z| < k_\mathrm{F}$ now describes a double Skyrmion texture with $N_{k_z} = \pm 2$. That is, the double Weyl points at $\mathbf{K}_\pm = (0, 0, \pm k_\mathrm{F})$ correspond to double (anti-)monopoles of the Berry curvature $\mathbf{F}(\mathbf{k})$, which is given by [44]

$$\begin{aligned} F_x(\mathbf{k}) &= \frac{2\Delta_0^2 k_x k_z (k_x^2 + k_y^2)}{\mu^2 \left[(k^2 - k_\mathrm{F}^2)^2 + \frac{\Delta_0^2}{\mu^2} (k_x^2 + k_y^2)^2 \right]^{\frac{3}{2}}}, \\ F_y(\mathbf{k}) &= \frac{2\Delta_0^2 k_y k_z (k_x^2 + k_y^2)}{\mu^2 \left[(k^2 - k_\mathrm{F}^2)^2 + \frac{\Delta_0^2}{\mu^2} (k_x^2 + k_y^2)^2 \right]^{\frac{3}{2}}}, \\ F_z(\mathbf{k}) &= \frac{2\Delta_0^2 (k_z^2 - k_\mathrm{F}^2)(k_x^2 + k_y^2)}{\mu^2 \left[(k^2 - k_\mathrm{F}^2)^2 + \frac{\Delta_0^2}{\mu^2} (k_x^2 + k_y^2)^2 \right]^{\frac{3}{2}}}. \end{aligned} \tag{17}$$

The Berry curvature is plotted in figure 2(b). As a result of the topological non-triviality, the d-wave Weyl superconductor (3)

supports two spin-degenerate, chirally dispersing arc surface states. (See figure 4(b). These surface states carry anomalous spin and thermal Hall currents.

3.3.3. Nodal noncentrosymmetric superconductor. Nodal NCSs defined by the BdG Hamiltonian $\mathcal{H}(\mathbf{k})$ in equation (5) satisfy time-reversal symmetry $T^{-1}\mathcal{H}(-\mathbf{k})T = +\mathcal{H}(\mathbf{k})$, with $T = \mathcal{K}\tau_0 \otimes \mathrm{i}\sigma_y$, and particle-hole symmetry $C^{-1}\mathcal{H}(-\mathbf{k})C = -\mathcal{H}(\mathbf{k})$, with $C = \mathcal{K}\tau_x \otimes \sigma_0$. Here, τ_i and σ_i are the Pauli matrices operating in particle-hole and spin space, respectively. Since $T^2 = -\mathbb{1}$ and $C^2 = +\mathbb{1}$, Hamiltonian (5) belongs to symmetry class DIII. According to table 1, the topological properties of class DIII Hamiltonians are characterized by $\mathbb{Z}_2$ topological numbers. While these binary invariants can give rise to protected Majorana cone surface states or arc surface states, they do not guarantee the stability of the superconducting nodes [61]. Hence, one might conclude that the superconducting nodes of the NCS (5) are unstable against gap opening. In addition to TRS and PHS, however, $\mathcal{H}(\mathbf{k})$ in Equation (5) also possesses the chiral symmetry $S^{-1}\mathcal{H}(\mathbf{k})S = -\mathcal{H}(\mathbf{k})$, with $S = -\tau_x \otimes \sigma_y$. Therefore, $\mathcal{H}(\mathbf{k})$ can be viewed as a member of symmetry class AIII and, as indicated by table 1, its line nodes are protected by a $\mathbb{Z}$ invariant, i.e. a winding number.

The $\mathbb{Z}_2$ and $\mathbb{Z}$ invariants of symmetry class DIII and AIII, respectively, can be conveniently expressed in terms of the off-diagonal block $q(\mathbf{k})$ of the spectral projector. For Hamiltonian (5), the matrix $q(\mathbf{k})$ takes the following form [21, 22]

$$q(\mathbf{k}) = \frac{1}{2\Lambda_{1,\mathbf{k}}\Lambda_{2,\mathbf{k}}}\Big[\left(\Lambda^+_{\mathbf{k}}B_{\mathbf{k}} - \Lambda^-_{\mathbf{k}}A_{\mathbf{k}}\,|\mathbf{l}_{\mathbf{k}}|\right)\sigma_0 + \left(\Lambda^+_{\mathbf{k}}A_{\mathbf{k}}\,|\mathbf{l}_{\mathbf{k}}| - \Lambda^-_{\mathbf{k}}B_{\mathbf{k}}\right)\frac{\mathbf{l}_{\mathbf{k}}}{|\mathbf{l}_{\mathbf{k}}|}\cdot\boldsymbol{\sigma}\Big]. \tag{18}$$

In equation (18) we have introduced the short-hand notation $A_{\mathbf{k}} = \lambda + \mathrm{i}\Delta_t$, $B_{\mathbf{k}} = \varepsilon_{\mathbf{k}} + \mathrm{i}\Delta_s$, and $\Lambda^\pm_{\mathbf{k}} = \Lambda_{1,\mathbf{k}} \pm \Lambda_{2,\mathbf{k}}$, where

$$\Lambda_{1,\mathbf{k}} = \sqrt{\left(\xi^+_{\mathbf{k}}\right)^2 + \left(\Delta^+_{\mathbf{k}}\right)^2} \quad \text{and} \quad \Lambda_{2,\mathbf{k}} = \sqrt{\left(\xi^-_{\mathbf{k}}\right)^2 + \left(\Delta^-_{\mathbf{k}}\right)^2} \tag{19}$$

are the positive eigenvalues of $\mathcal{H}(\mathbf{k})$. The unitary matrix $q(\mathbf{k}) \in U(2)$ is constrained by time-reversal symmetry as $\mathrm{i}\sigma_y q^{\mathrm{T}}(-\mathbf{k}) = q(\mathbf{k})\mathrm{i}\sigma_y$.

Winding number. The stability of the line nodes of NCS (5) is ensured by the conservation of the winding number [19, 21, 57, 68, 69]

$$W_{\mathcal{L}} = \frac{1}{2\pi i}\oint_{\mathcal{L}} \mathrm{d}k_l\,\mathrm{Tr}[q^\dagger(\mathbf{k})\partial_{k_l}q(\mathbf{k})], \tag{20}$$

where $\mathcal{L}$ is a closed one-dimensional contour parametrized by k_l, which interlinks with a line node. Mathematically speaking, equation (20) labels the homotopy classes of mappings from $\mathcal{L} \simeq S^1 \to q(\mathbf{k}) \in U(2)$. Since the first homotopy group of $U(2)$ equals the group of the integer numbers $\mathbb{Z}$ [67], i.e. $\pi_1[U(2)] = \mathbb{Z}$, the winding number $W_{\mathcal{L}}$ can in principle take on any integer value. Using equation (18), we find that $W_{\mathcal{L}}$ for the BdG Hamiltonian (5) can be rewritten in the simpler form

$$W_{\mathcal{L}} = \frac{1}{2\pi}\oint_{\mathcal{L}} \mathrm{d}k_l\,\partial_{k_l}\left[\arg\left(\xi^+_{\mathbf{k}} + \mathrm{i}\Delta^+_{\mathbf{k}}\right) + \arg\left(\xi^-_{\mathbf{k}} + \mathrm{i}\Delta^-_{\mathbf{k}}\right)\right]. \tag{21}$$

Assuming that the superconducting gaps $\Delta^\pm_{\mathbf{k}}$ of Hamiltonian (5) are nonzero only in the vicinity of the Fermi surfaces (which is the case for weak-pairing superconductors), equation (21) can be further simplified to [22]

$$W_{\mathcal{L}} = -\frac{1}{2}\sum_{\nu=\pm}\sum_{\mathbf{k}_0\in S^\nu_{\mathcal{L}}} \mathrm{sgn}\left(\partial_{k_l}\xi^\nu_{\mathbf{k}}\big|_{\mathbf{k}=\mathbf{k}_0}\right)\mathrm{sgn}\left(\Delta^\nu_{\mathbf{k}_0}\right). \tag{22}$$

The second sum in equation (22) is over the set of points $S^\nu_{\mathcal{L}}$ given by the intersection of the ν-helicity Fermi surface with the one-dimensional contour $\mathcal{L}$. Equation (22) demonstrates that for a weak-pairing nodal superconductor of the form (5), the topological characteristics of the nodal structure is entirely determined by the phases of the gaps in the neighborhood of the positive- and negative-helicity Fermi surfaces. This is in complete agreement with the discussion of section 4.3.

By the bulk-boundary correspondence [64], a non-zero value of $W_{\mathcal{L}}$ signals the appearance of zero-energy states at the surface of the NCS. To make this more explicit, let us consider a contour $\mathcal{L}$ along a line parallel to the (lmn) direction in the bulk Brillouin zone. (See figure 3). With this choice we obtain for equation (22)

$$W_{(lmn)}(\mathbf{k}_\parallel) = -\frac{1}{2}\sum_{\nu=\pm}\left[\mathrm{sgn}\left(\Delta^\nu_{\mathbf{k}_\nu}\right) - \mathrm{sgn}\left(\Delta^\nu_{\mathbf{k}'_\nu}\right)\right], \tag{23}$$

where $\mathbf{k}_\parallel$ denotes the momentum perpendicular to the (lmn) direction, and $\mathbf{k}_\pm = (\mathbf{k}_\parallel, k_{\perp,\pm})$ and $\mathbf{k}'_\pm = (\mathbf{k}_\parallel, k'_{\perp,\pm})$

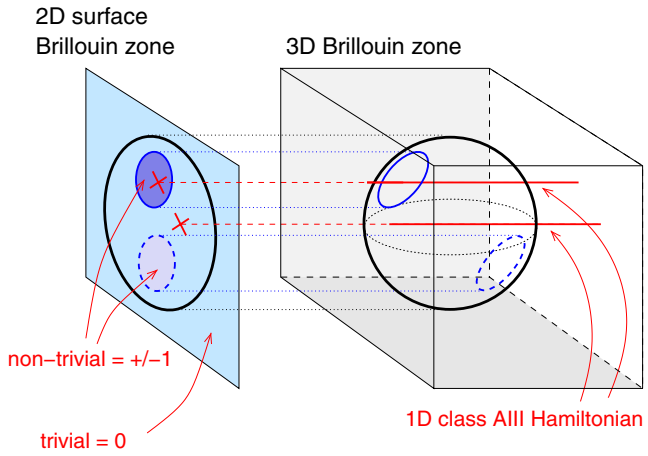

Figure 3. The relationship of the bulk gap structure to the surface states of a nodal topological superconductor. The left part of the figure shows the surface Brillouin zone with the projected Fermi surface indicated in black. Flat-band surface states occur within the two regions bounded by the projected nodal lines (dark blue and light gray areas). Within these two regions the winding number (23) takes on the values $W = \pm 1$, while outside these regions it is zero; the bulk Hamiltonians restricted to a surface momentum in these regions (red lines in 3D Brillouin zone) belong to symmetry class AIII and are topologically trivial and nontrivial, respectively. The right part of the figure shows the three-dimensional bulk Brillouin zone with a spherical Fermi surface (black ellipse) and two nodal rings (solid and dashed blue ellipses).

are momenta on the positive- and negative-helicity Fermi surfaces which project onto $\mathbf{k}_\parallel$, where $k_{\perp,\pm}$ and $k'_{\perp,\pm}$ have opposite signs. With this, it follows from the bulk-boundary correspondence that zero-energy states appear at the (lmn) face of the NCS whenever $W_{(lmn)}(\mathbf{k}_\parallel) \neq 0$. This corresponds to regions of the surface Brillouin zone that are bounded by the projected nodal rings of the bulk gap. (See figure 3). In other words, the non-trivial topology of the nodal rings in the bulk leads to protected flat-band surface states (see figure 1(c) and section 4.3.3).

$\mathbb{Z}_2$ topological invariant. The one-dimensional (two-dimensional) $\mathbb{Z}_2$ invariant of symmetry class DIII is given by [4, 20, 21, 70, 71]

$$N_{\mathcal{L}} = \prod_{\mathbf{K}\in\mathcal{L}} \frac{\mathrm{Pf}\left[\mathrm{i}\sigma_y q^{\mathrm{T}}(\mathbf{K})\right]}{\sqrt{\det\left[\mathrm{i}\sigma_y q^{\mathrm{T}}(\mathbf{K})\right]}}, \tag{24}$$

where Pf is the Pfaffian and the product is over the two (four) time-reversal invariant momenta $\mathbf{K}$ of the one-dimensional (two-dimensional) centrosymmetric contour $\mathcal{L}$. In order for $N_{\mathcal{L}}$ to be well defined, the contour $\mathcal{L}$ needs to be centrosymmetric (i.e. mapped onto itself under $\mathbf{k} \to -\mathbf{k}$) and must not intersect with the nodes of $\mathcal{H}(\mathbf{k})$. Inspection of equation (24) reveals that $N_{\mathcal{L}}$ can only take on the values ± 1, where -1 (+1) indicates a topologically nontrivial (trivial) character. For weak-pairing superconductors the gaps $\Delta^{\pm}_{\mathbf{k}}$ are non-zero only in a small neighborhood of the Fermi surface and hence equation (24) can be simplified to [22]

$$N_{\mathcal{L}} = \mathrm{sgn}\left(\Delta^{+}_{\mathcal{L}}\right)\mathrm{sgn}\left(\Delta^{-}_{\mathcal{L}}\right), \tag{25}$$

where $\mathrm{sgn}\left(\Delta^{\pm}_{\mathcal{L}}\right)$ represents the sign of the gap at the intersection of $\mathcal{L}$ with the positive/negative helicity Fermi surface. By the bulk-boundary correspondence [65], $N_{\mathcal{L}} = -1$ for a one-dimensional contour $\mathcal{L}$ indicates the appearance of a helical Majorana cone at a surface of the NCS. (See figure 1(a)). Similarly, for a two-dimensional contour $\mathcal{L}$, $N_{\mathcal{L}} = -1$ gives rise to an arc surface state. (See figure 1(b).

3.4. Crystalline topological nodal superconductors

In the previous subsections we have discussed the topological classification of nodal superconductors in terms of internal symmetries, i.e. global symmetries that act locally in position space (see table 1). Recently it became apparent that besides global symmetries, crystal symmetries which operate non-locally in position space can also lead to the protection of superconducting nodes [60, 61, 72–75]. Indeed, a complete topological classification of reflection-symmetry-protected nodal superconductors was recently obtained in [61]. Moreover, it has been argued that the heavy fermion superconductor UPt_3 can be viewed as a crystalline topological nodal superconductor, since its topological surface states are protected by mirror symmetry [76].

4. Bound state wavefunctions

In this section we construct the wavefunctions of the surface states of a topological superconductor within an approximate low-energy effective theory. Such so-called 'quasiclassical' methods are a standard technique in the study of inhomogeneous superconductivity [77–80]. The focus here is to demonstrate how this approach can be used to explore the surface physics of topological superconductors.

4.1. Deriving the low-energy theory

We consider the surface of a topological superconductor, with normal defining the axis $r_\perp$. The superconductor is assumed to occupy the half-space $r_\perp > 0$, and translational invariance parallel to the surface ensures that the transverse momentum $\mathbf{k}_\parallel$ is a good quantum number. Our aim is to solve the BdG equation

$$\tilde{H}\Psi(\mathbf{k}_\parallel; r_\perp) = E\Psi(\mathbf{k}_\parallel; r_\perp) \tag{26}$$

for states with energy comparable to the superconducting gap. The Hamiltonian $\tilde{H}(\mathbf{k}_\parallel)$ appearing here is related to the bulk Hamiltonian $H(\mathbf{k})$ by

$$\tilde{H}(\mathbf{k}_\parallel) = \int \frac{\mathrm{d}k_\perp}{2\pi} H(\mathbf{k})\mathrm{e}^{\mathrm{i}k_\perp r_\perp}. \tag{27}$$

The BdG equations can be solved numerically, e.g. by exact diagonalization of a lattice regularization of the Hamiltonian. Superconductivity is a low-energy phenomenon, however, where the characteristic energy scale of the gap Δ is typically much smaller than the Fermi energy E_{F}, and it is at such low energy scales that the surface states exist. Not only is it computationally advantageous to restrict our solution of equation (26) to the low-energy sector, but it also permits at least semi-analytic solutions which provide a more transparent understanding of the physics. This is the motivation for the quasiclassical theory of superconductivity. A full development of this theory, in particular the construction of the quasiclassical Green's function and the self-consistent determination of the pairing potential, is rather involved and beyond the scope of this review. We therefore sketch the theory below, and refer interested readers to the extensive literature on the subject, e.g. [77–81].

The first step in constructing an effective theory is to bring the noninteracting Hamiltonian $h(\mathbf{k})$ into a diagonal form. The low-energy quasiparticle excitations in the superconductor occur within a narrow momentum shell about the normal-state Fermi surface of width $\sim \Delta/\hbar|\mathbf{v}_{\mathrm{F}}| \ll |\mathbf{k}_{\mathrm{F}}|$ where $\mathbf{v}_{\mathrm{F}}$ is the Fermi velocity. The Fermi velocity is regarded as constant across this momentum shell, which allows us to linearize the low-energy Hamiltonian $[h(\mathbf{k})]_{\alpha,\alpha} \approx \hbar\mathbf{v}_{\mathrm{F},\alpha}\cdot(\mathbf{k}-\mathbf{k}_{\mathrm{F},\alpha})$ where $\mathbf{k}_{\mathrm{F},\alpha}$ lies on the Fermi surface of the α band. We now examine the pairing matrix $\hat{\Delta}(\mathbf{k})$. The superconducting gap is taken to be constant along the direction of the Fermi velocity at each point on the Fermi surface, i.e. $\hat{\Delta}(\mathbf{k}) \approx \hat{\Delta}(\mathbf{k}_{\mathrm{F},\alpha})$. The solution of the low-energy effective theory is therefore only sensitive to the value of the superconducting gap in the immediate vicinity of the Fermi surface. Pairing between states on nondegenerate Fermi surfaces is not considered.

An appropriate ansatz for an eigenstate of the low-energy Hamiltonian is

$$\Psi(\mathbf{k}_\parallel;\mathbf{r}) = \sum_j a_j \begin{pmatrix}\mathbf{u}_j\\ \mathbf{v}_j\end{pmatrix} e^{i(\mathbf{k}_\parallel\cdot\mathbf{r}_\parallel+[k_j+\delta k_j]r_\perp)}, \tag{28}$$

where the sum j is over all scattering channels, a_j are $\mathbb{C}$-number coefficients, the vector $\mathbf{k}_j = (\mathbf{k}_\parallel, k_j)$ lies on the Fermi surface, $|\delta k_j| \ll |k_j|$ is a small energy-dependent deviation from the Fermi wavevector $\mathbf{k}_j$, and the multi-component BCS coherence factors $\mathbf{u}_j$ and $\mathbf{v}_j$ are functions only of $\mathbf{k}_j$ and the energy. The coefficients a_j in equation (28) are determined by imposing boundary conditions on the wavefunction at the surface, which can in principle be derived from the underlying microscopic theory. This presents the greatest challenge faced by the low-energy effective theory, as there is no general prescription of how this should be done, especially for multiband systems or those with strong spin-orbital mixing.

In order to avoid this complication, in the following we restrict our attention to a commonly-used microscopic model of the normal state where boundary conditions can be explicitly and easily derived [1, 14, 15, 22, 23, 31, 34, 45, 78, 80, 82–88]. Specifically, we adopt the noninteracting Hamiltonian

$$h(\mathbf{k}) = \left(\frac{\hbar^2}{2m}|\mathbf{k}|^2 - \mu\right)\hat{\sigma}_0 + \lambda\mathbf{l}_\mathbf{k}\cdot\hat{\boldsymbol{\sigma}} + V_{\text{work}}\Theta(r_\perp) \tag{29}$$

This describes a free electron gas, including antisymmetric SOC of strength λ so as to model both centrosymmetric ($\lambda = 0$) and noncentrosymmetric ($\lambda \neq 0$) systems. In the latter case, the spin–orbit vector $\mathbf{l}_\mathbf{k}$ has the following continuum-limit representations for the different point groups

$$\mathbf{l}_\mathbf{k} = \begin{cases} (a_1k_x + a_2k_y)\mathbf{x} + (a_3k_x + a_4k_y)\mathbf{y} + a_5k_z\mathbf{z}, & C_2\\ k_y\mathbf{x} - k_x\mathbf{y}, & C_{4v}\\ k_x(1 + g_2[k_y^2 + k_z^2])\mathbf{x} & \\ \quad +k_y(1 + g_2[k_x^2 + k_z^2])\mathbf{y} + k_z(1 + g_2[k_x^2 + k_y^2])\mathbf{z}, & \mathcal{O}\\ k_x(k_y^2 - k_z^2)\mathbf{x} + k_y(k_z^2 - k_x^2)\mathbf{y} + k_z(k_x^2 - k_y^2)\mathbf{z}, & T_d \end{cases} \tag{30}$$

The coefficients $a_{j=1,\ldots,5}$ and g_2 appearing in the expressions for the C_2 and $\mathcal{O}$ point groups are arbitrary. Our Hamiltonian also includes a confining potential V_{work} for the surface which we identify with the work function. For our low-energy theory it is reasonable to take the limit $V_{\text{work}} \to \infty$, and so we implicitly include this potential as the boundary condition that the wavefunctions vanish at the surface.

4.2. Bound states of Weyl superconductors

As an illustration of the quasiclassical method, we consider the subgap bound states appearing at the (1 0 0) surface of the Weyl superconductor models introduced in section 2.1. Take a point $\mathbf{k}_\parallel = (k_y, k_z)$ in the two-dimensional surface Brillouin zone that lies within the projection of the Fermi surface, i.e. $|\mathbf{k}_\parallel| < k_\text{F}$. This surface wavevector corresponds to two points on the Fermi surface $\mathbf{p} = (k_x, \mathbf{k}_\parallel)$ and $\mathbf{p}' = (-k_x, \mathbf{k}_\parallel)$, where $k_x = \sqrt{k_\text{F}^2 - |\mathbf{k}_\parallel|^2}$. The bound state wavefunction is then a superposition of evanescent states at these momenta

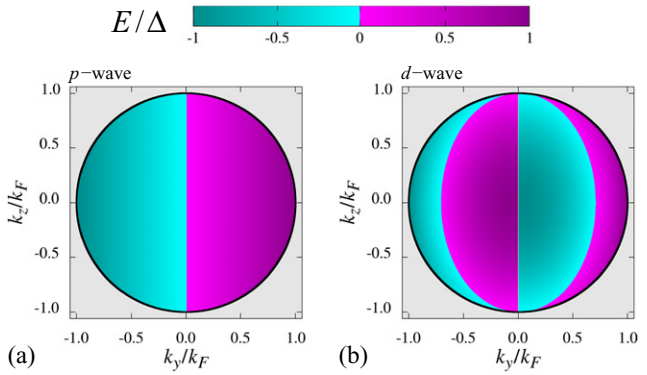

Figure 4. Topological surface states in Weyl superconductors. The surface bound-state spectra are plotted as a function of the (1 0 0) surface momentum (k_y, k_z) for (a) the $(p_x + ip_y)$-wave and (b) the $(d_{x^2-y^2} + id_{xy})$-wave Weyl superconductor. The energy of the bound states is indicated by the color scale, where the jump from cyan to magenta occurs at zero energy; light grey indicates the absence of a surface state. The thick black line shows the projection of the Fermi surface.

$$\Psi(\mathbf{k}_\parallel;\mathbf{r}) = \left\{a_\mathbf{p}\begin{pmatrix}1\\ \gamma_\mathbf{p}\end{pmatrix}e^{(ik_x-\kappa_\mathbf{p})x} + a_{\mathbf{p}'}\begin{pmatrix}1\\ \gamma_{\mathbf{p}'}\end{pmatrix}e^{-(ik_x+\kappa_{\mathbf{p}'})x}\right\}e^{i\mathbf{k}_\parallel\cdot\mathbf{r}} \tag{31}$$

where $a_\mathbf{k}$ are $\mathbb{C}$-number coefficients, and the coherence factors $\gamma_\mathbf{k}$ and inverse decay length $\kappa_\mathbf{k}$ are defined

$$\gamma_\mathbf{k} = \frac{1}{\Delta_\mathbf{k}}\left[E - i\,\text{sgn}(k_x)\sqrt{|\Delta_\mathbf{k}|^2 - E^2}\right], \tag{32}$$

$$\kappa_\mathbf{k} = \frac{m\sqrt{|\Delta_\mathbf{k}|^2 - E^2}}{\hbar^2|k_x|}. \tag{33}$$

The ansatz equation (31) satisfies the criteria that the wavefunction vanishes in the bulk. The requirement that the wavefunction also vanishes at the surface leads to the condition on the coherence factors

$$\gamma_\mathbf{p} - \gamma_{\mathbf{p}'} = 0. \tag{34}$$

This can be analytically solved for the surface bound state energies of the p-wave and d-wave Weyl superconductor:

$$E(\mathbf{k}_\parallel) = \begin{cases} \Delta_0\left(1 - \tilde{k}_z^2\right)^{1/2}\tilde{k}_y & p_x + ip_y\\ \Delta_0\left(1 - \tilde{k}_z^2\right)\left(1 - |\tilde{\mathbf{k}}_\parallel|^2 - \tilde{k}_y^2\right) & \\ \quad\times\text{sgn}(\tilde{k}_y) & d_{x^2-y^2} + id_{xy} \end{cases} \tag{35}$$

where $\tilde{k}_\mu = k_\mu/k_\text{F}$. The bound state spectrum is plotted in figure 4. In both cases, we observe zero-energy arc surface states running between the nodes at the north and south poles of the Fermi surface. Whereas there is only a single such arc state in the p-wave Weyl superconductor, there are two arc states in the d-wave Weyl superconductor, consistent with the Chern numbers equation (15) of $N_{k_z} = 1$ and $N_{k_z} = 2$ for $|k_z| < k_\text{F}$, respectively.

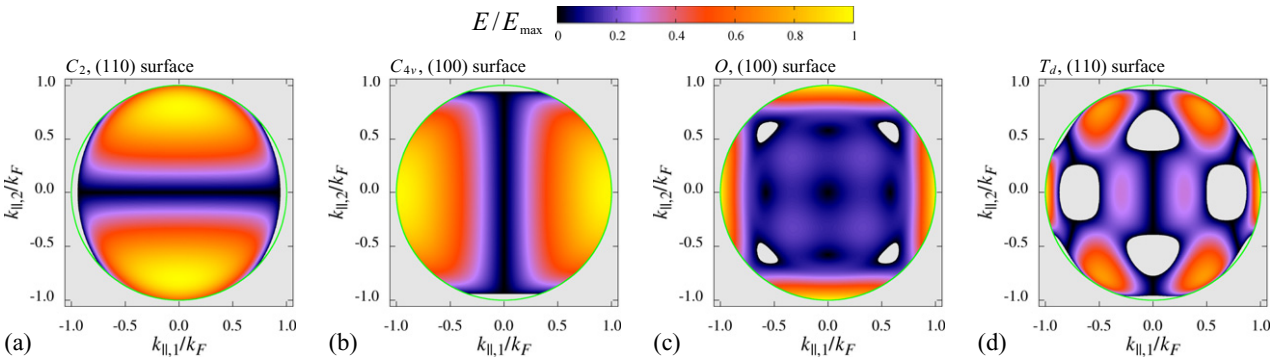

Figure 5. Helical Majorana and arc states in NCS. The surface bound-state spectra are plotted as a function of surface momentum $\mathbf{k}_\parallel$ for: (a) (1 1 0) face of C_2 NCS with $r = 0.4$ and $a_{i=1,\ldots,5} = 1$; (b) (1 0 0) face of C_{4v} NCS with $r = 0.25$; (c) (1 0 0) face of O NCS with $r = 0.1$ and $g_2 = -1.5$; (d) (1 1 0) face of T_d NCS with $r = 0.2$. The energy of the bound states is indicated by the color scale, where black corresponds to zero energy and yellow to the maximum energy $E_{\max}$; light grey indicates the absence of a surface state. The light green line shows the projection of the Fermi surface. As discussed in the text, in each case the zero-energy state at $\mathbf{k}_\parallel = 0$ is a topological helical Majorana. The C_2 and C_{4v} NCS also display topologically-protected arc states.

4.3. Bound states of NCS

We now turn our attention to the surface bound states of a NCS. We restrict ourselves to the limit $E_F \gg \lambda \max\{|\mathbf{l}_\mathbf{k}|\} \gg |\Delta|$, so that we can ignore the spin-splitting of the Fermi surfaces in the low-energy theory, but the triplet $\mathbf{d}$-vector is still constrained to be parallel to the SOC vector, i.e. $\mathbf{d}_\mathbf{k} = \Delta_t \mathbf{l}_\mathbf{k}$, and hence the physical description outlined in section 2.2 is still applicable. This is a common approximation [22, 23, 80, 88–93] as accounting for the spin-orbit splitting of the Fermi surfaces complicates the analysis but generally only quantitatively modifies the surface state spectra.

A similar (but more involved) argument to that for the Weyl superconductors above gives the implicit equation [22, 23, 80] for the bound states energies

$$0 = (\gamma^+_{\mathbf{p}'} - \gamma^-_{\mathbf{p}})(\gamma^-_{\mathbf{p}'} - \gamma^+_{\mathbf{p}})(|\mathbf{l}_\mathbf{p}||\mathbf{l}_{\mathbf{p}'}| - \mathbf{l}_\mathbf{p} \cdot \mathbf{l}_{\mathbf{p}'}) + (\gamma^+_{\mathbf{p}'} - \gamma^+_{\mathbf{p}})(\gamma^-_{\mathbf{p}'} - \gamma^-_{\mathbf{p}})(|\mathbf{l}_\mathbf{p}||\mathbf{l}_{\mathbf{p}'}| + \mathbf{l}_\mathbf{p} \cdot \mathbf{l}_{\mathbf{p}'}). \quad (36)$$

where

$$\gamma^\pm_\mathbf{k} = \frac{1}{\Delta^\pm_\mathbf{k}}\left[E - \mathrm{i}\,\mathrm{sgn}(v_{\mathrm{F},\perp}(\mathbf{k}))\sqrt{|\Delta^\pm_\mathbf{k}|^2 - E^2}\right] \quad (37)$$

where $v_{\mathrm{F},\perp}(\mathbf{k})$ is the component of the Fermi velocity in the direction normal to the boundary. Bound-state energies must lie within the minimum gap, i.e. $|E| < \min\{|\Delta^\pm_\mathbf{p}|, |\Delta^\pm_{\mathbf{p}'}|\}$. Although the general solution must be obtained numerically, analytic conditions can be derived for the existence of zero-energy states. Substituting the zero-energy form of $\gamma^\pm_\mathbf{k} = -\mathrm{i}\,\mathrm{sgn}(v_{\mathrm{F},\perp}(\mathbf{k})\Delta^\pm_\mathbf{k})$ into equation (36) we obtain five conditions for zero-energy states in terms of the SOC vector and the gap signs [22]:

(a) The spin-orbit vectors $\mathbf{l}_\mathbf{p}$ and $\mathbf{l}_{\mathbf{p}'}$ are parallel, and the gap signs satisfy $\mathrm{sgn}(\Delta^+_\mathbf{p}) = \mathrm{sgn}(\Delta^-_{\mathbf{p}'}) \neq \mathrm{sgn}(\Delta^+_{\mathbf{p}'}) = \mathrm{sgn}(\Delta^-_\mathbf{p})$.

(b) The spin-orbit vectors $\mathbf{l}_\mathbf{p}$ and $\mathbf{l}_{\mathbf{p}'}$ are antiparallel, and the gap signs satisfy $\mathrm{sgn}(\Delta^+_\mathbf{p}) = \mathrm{sgn}(\Delta^+_{\mathbf{p}'}) \neq \mathrm{sgn}(\Delta^-_{\mathbf{p}'}) = \mathrm{sgn}(\Delta^-_\mathbf{p})$.

(c) The gap signs satisfy $\mathrm{sgn}(\Delta^+_\mathbf{p}) = \mathrm{sgn}(\Delta^+_{\mathbf{p}'})$ and $\mathrm{sgn}(\Delta^-_{\mathbf{p}'}) \neq \mathrm{sgn}(\Delta^-_\mathbf{p})$.

(d) The gap signs satisfy $\mathrm{sgn}(\Delta^+_\mathbf{p}) \neq \mathrm{sgn}(\Delta^+_{\mathbf{p}'})$ and $\mathrm{sgn}(\Delta^-_{\mathbf{p}'}) = \mathrm{sgn}(\Delta^-_\mathbf{p})$.

(e) The gap signs satisfy $\mathrm{sgn}(\Delta^+_\mathbf{p}) \neq \mathrm{sgn}(\Delta^+_{\mathbf{p}'})$, $\mathrm{sgn}(\Delta^-_{\mathbf{p}'}) \neq \mathrm{sgn}(\Delta^-_\mathbf{p})$, $\mathrm{sgn}(\Delta^-_{\mathbf{p}'}) \neq \mathrm{sgn}(\Delta^+_\mathbf{p})$, and $\mathrm{sgn}(\Delta^+_{\mathbf{p}'}) \neq \mathrm{sgn}(\Delta^-_\mathbf{p})$.

These five conditions for a zero-energy state include the topological criteria defined in section 3.3.3. Only a state satisfying the first condition is not topological: It cannot be a Kramers-degenerate Majorana mode as the antisymmetric spin-orbit vectors at $\mathbf{p}$ and $\mathbf{p}'$ are not parallel if $\mathbf{k}_\parallel$ lies at a time-reversal invariant point in the surface Brillouin zone; It also cannot be an arc surface state protected by a $\mathbb{Z}_2$ number, since the condition on the gap signs requires that there be a node in the plane defined by $\mathbf{p}$ and $\mathbf{p}'$. On the other hand, since condition (b) requires different sign of the positive and negative helicity gaps, it is clearly consistent with the definition of the topological number equation (25) for both these topological states. It also describes nontopological states, however, as these conditions are not sufficiently restrictive. The conditions (c)–(e) exclusively describe flat band states with nontrivial winding number, and they are equivalent to the topological criteria equation (23). Specifically, conditions (c) and (d), which correspond to a situation where only one of the helical gaps has a sign change between the two sides of the Fermi surface, describe topologically protected nondegenerate zero-energy states with winding number $W_{(lmn)} = \pm 1$. In contrast, (e) requires sign changes of both helical gaps and gives doubly degenerate states of winding number $W_{(lmn)} = \pm 2$.

4.3.1. Helical Majorana. Helical Majorana states appearing at the centre of the surface Brillouin zone ($\mathbf{k}_\parallel = 0$) are relatively common for majority-triplet NCS at high-symmetry surfaces. In each of the examples shown in figure 5 the zero-energy state at the zone centre has this topological protection. The other zero-energy states that are present elsewhere in the surface Brillouin zone in each of these examples, on the other hand, do not satisfy the necessary criterion.

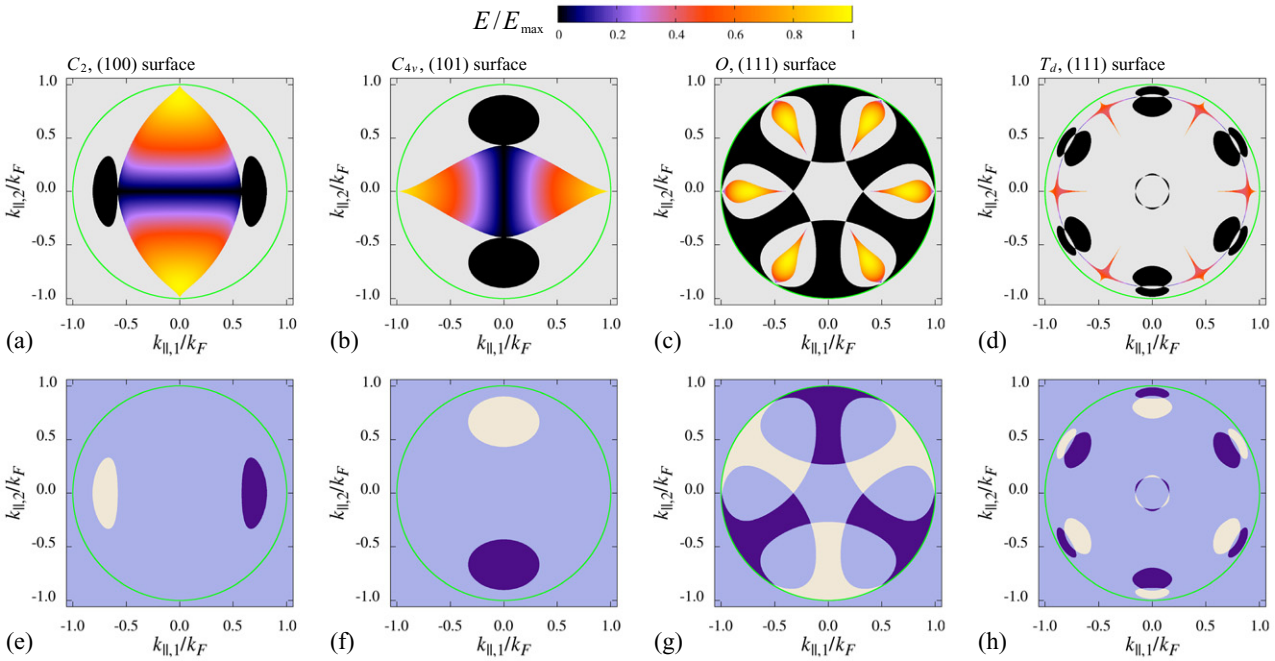

Figure 6. Topological flat-band states in nodal NCS. In the top row we plot the surface bound-state spectrum as a function of surface momentum $\mathbf{k}_\parallel$ for (a) the (1 0 0) surface of a C_2 NCS with $r = 0.25$ and $a_{i=1,\ldots,5} = 1$, (b) the (1 0 1) face of a C_{4v} NCS with $r = 0.25$, (c) the (1 1 1) face of O NCS with $r = 0.25$ and $g_2 = -1.5$, (d) and the (1 1 1) face of T_d NCS with $r = 0.15$. The colour scale is the same as in figure 5. In the bottom row we plot the corresponding variation of the $W_{(lmn)}(\mathbf{k}_\parallel)$. Dark blue (gray) corresponds to $W_{(lmn)}(\mathbf{k}_\parallel) = +1\ (-1)$, while light blue represents. $W_{(lmn)}(\mathbf{k}_\parallel) = 0$. Figures (a)–(c) adapted from [85].

4.3.2. Arc states. Topologically protected arc states are rare, as the condition that $\mathbf{l}_\mathbf{k}$ be symmetric upon reflection about some plane places severe constraints on the point group symmetry. There are two examples in figure 5: portions of the arc states at the (1 1 0) surface of the C_{2v} NCS shown in panel (a), and the entire line of zero energy states connecting the projection of the nodal rings at the (1 0 0) surface of the C_{4v} NCS in panel (b). In contrast, the arc states at the (1 1 0) surface of the T_d NCS (panel (d)) do not have topological protection, as the topological condition only holds for planes which intersect gap nodes.

4.3.3. Flat-band states. Flat-band states are the most generic topological surface state of nodal NCSs, appearing at any surface where the projections of the nodal rings enclose a finite area and do not exactly lie on top of another. We illustrate this with an example from each point group in figure 6. In the top row we plot the spectrum in the surface Brillouin zone, while in the bottom row we show the corresponding variation of the winding number $W_{(lmn)}(\mathbf{k}_\parallel)$. The regions where the topological number evaluates to ± 1 are bounded by the projected line nodes of the gap, and exactly matches the location of the zero-energy flat bands in the surface spectrum. By the bulk-boundary correspondence this ensures the topological protection of the zero-energy flat bands and implies that these states are nondegenerate.

4.3.4. Spin polarisation of surface states. The surface bound states of NCSs typically display a strong spin polarization, which is a consequence of the broken inversion symmetry. The μ-component of the spin polarization of a bound state at transverse momentum $\mathbf{k}_\parallel$ and energy E is defined [85] as the expectation value

$$\rho^\mu(E, \mathbf{k}_\parallel) = \int_0^\infty \mathrm{d}r_\perp \Psi^\dagger(\mathbf{k}_\parallel; r_\perp) \begin{pmatrix} \hat{\sigma}^\mu & 0 \\ 0 & -[\hat{\sigma}^\mu]^* \end{pmatrix} \Psi(\mathbf{k}_\parallel; r_\perp) \tag{38}$$

where $\Psi(\mathbf{k}_\parallel; r_\perp)$ is the wavefunction. Due to the symmetries of the Hamiltonian (time-reversal, particle-hole, and chiral), the polarization of the edge states is even in energy and odd in the surface momentum, i.e. $\rho^\mu(E, \mathbf{k}_\parallel) = \rho^\mu(-E, \mathbf{k}_\parallel) = -\rho^\mu(E, -\mathbf{k}_\parallel)$, and there is no spin accumulation at the surface. The spin polarization is sometimes defined only with reference to the electron-like components of the wavefunction [86, 89, 90], but the definition equation (38) is more reasonable as this quantity couples to an applied Zeeman field.

The spin polarization of the edge states at the (1 0 1) surfaces of a C_{4v} NCS is shown in figure 7. Both the dispersing and the flat-band edge states display a pronounced spin texture. The spin polarization does not follow from the topology, however, but rather arises from the unequal contribution of positive- and negative-helicity states to the wavefunction. The spin polarization of the surface states must match that of the continuum states where the two intersect, in particular at the bounding nodes of the flat band states. Despite its nontopological origin, the spin polarization of the topological flat-band states is exploited in several proposed experimental tests of their existence.

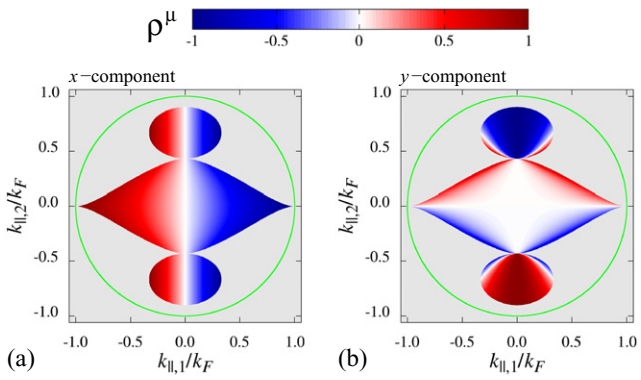

Figure 7. Spin polarization of the surface states at the (1 0 1) surface of a C_{4v} point group NCS with $r = 0.25$. Panels (a) and (b) show the spin polarization along the x- and y- axes of the crystal, respectively. The z-spin polarization is vanishing. The energy of the states is shown in figure 6(b). Figure adapted from [85].

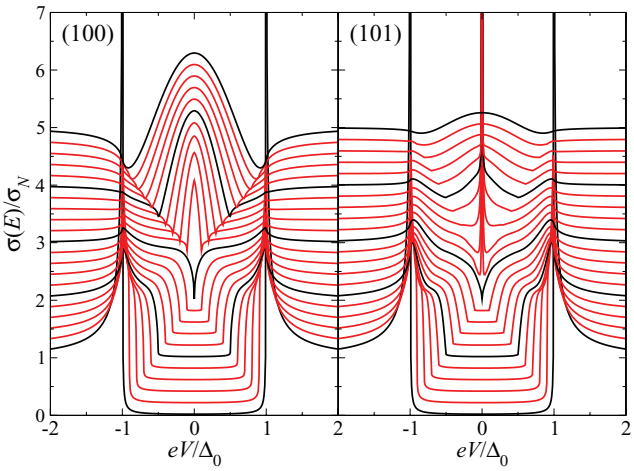

Figure 8. Tunneling-conductance spectra at the (1 0 0) and (1 0 1) interfaces of a C_{4v} NCS with tunneling barrier strength $Z = 4$. The results are normalized by the normal state conductance σ_N in the absence of superconductivity. In both panels the singlet-triplet parameter r is tuned from $r = 0$ (purely triplet) at the top to $r = 1$ (purely singlet) at the bottom in steps of 0.05. The curves at $r = 0$, 0.25, 0.5, 0.75, and 1 are highlighted in black. The conductance spectra are offset by 0.2 for clarity.

5. Experimental signatures of topological surface states

Directly detecting the surface states of a topological superconductor requires measurement techniques sensitive to the surface properties. This is a much greater experimental challenge than demonstrating the existence of gap nodes in the bulk, as it generally requires the preparation of high-quality surfaces or the incorporation of the topological superconductor into a heterostructure device. These hurdles are not insurmountable, however, as evidenced by the observation of surface states in unconventional superconductors such as the cuprates [94–96] and Sr_2RuO_4 [97]. In this section we examine different experimental signatures of topological surface states.

5.1. Tunneling conductance

Conductance spectroscopy experiments represent the dominant approach to probing the surface states of unconventional superconductors [78, 98, 99]. Since the conductance is sensitive to the surface density of states of the superconductor, it can provide direct evidence of surface states. A number of authors have studied the conductance signatures of topologically protected surface states of NCS [22–24, 31, 45, 80, 84, 85, 91, 100–103].

The simplest model of a conductance experiment consists of a junction between a topological superconductor and a normal metal with an insulating barrier at their interface. The conductance $\sigma_S(E)$ at zero temperature is given by a generalization of the familiar Blonder–Tinkham–Klapwijk formula [101, 104],

$$\sigma_S(E) = \sum_{\mathbf{k}_\|} \left\{ 1 + \frac{1}{2} \sum_{\sigma,\sigma'} \left(|a^{\sigma,\sigma'}_{\mathbf{k}_\|}|^2 - |b^{\sigma,\sigma'}_{\mathbf{k}_\|}|^2 \right) \right\}, \qquad (39)$$

where $a^{\sigma,\sigma'}_{\mathbf{k}_\|}$ and $b^{\sigma,\sigma'}_{\mathbf{k}_\|}$ are the Andreev and normal reflection coefficients, respectively, for spin-σ electrons injected into the superconductor at interface momentum $\mathbf{k}_\|$. In the presence of SOC, both spin-preserving ($\sigma' = \sigma$) and spin-flip ($\sigma' = -\sigma$) Andreev and normal reflection coefficients are included. The scattering coefficients are determined by solution of the BdG equation for an electron at bias energy $E = eV$ injected into the superconductor from the normal lead. The insulating tunneling barrier is commonly modeled as a δ-function with strength $U = ZE_F/k_F$ [78]. The value of the dimensionless barrier parameter Z defines different experimental regimes: small values of $Z < 1$ are least sensitive to surface states, and are typically used to model point contact Andreev spectroscopy experiments [105]; larger values $Z \gtrsim 1$ give clear signatures of the surface states and are characteristic of tunnel junctions and scanning tunneling microscopy. We will concentrate upon the latter regime.

Tunneling conductance spectra at the (1 0 0) and (1 0 1) interfaces of a C_{4v} NCS are shown in figure 8. While the majority-singlet cases ($r > 0.5$) show a clear gap feature, majority-triplet pairing ($r < 0.5$) is characterized by substantial subgap conductance due to resonant tunneling through the surface states. At the (1 0 0) interface, the dispersing arc states give a broad feature centred at zero bias which completely fills the gap. This is also present at the (1 0 1) interface, but here the most striking aspect is the sharp zero-bias conductance peak due to tunneling into the zero-energy flat-band states [78]. The sharp zero-bias peak is a robust indicator of the flat-bands, as it arises from their singular contribution to the surface density of states. On the other hand, fine structures in the dispersing states give rise to a much richer variation in their contribution to the conductance, and there is no universal signature [23, 80]. In particular, there is no way to distinguish the dispersing surface states of a NCS from those of a Weyl superconductor using simple tunneling conductance measurements.

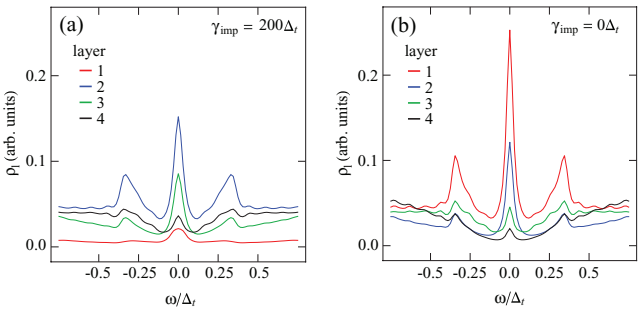

Figure 9. Layer-resolved local density of states ρ_l of a $(d_{xy} + p)$-wave NCS in a ribbon geometry with (0 1) edges, which displays zero-energy flat bands. Panel (a) corresponds to a dirty NCS with non-magnetic Gaussian disorder in the outermost layer of strength $\gamma_{\rm imp} = 200\Delta_t$, while panel (b) represents a clean NCS. In the former, the outermost layer is 'dead' and the topologically protected edge states develop in the second layer. Figure adapted from [113].

Many variations on the basic junction geometry are possible, e.g. replacing the normal lead by a metallic ferromagnet [93, 103, 106], or assuming a spin-active barrier [85]. This allows conductance measurements to probe the spin structure and, indirectly, the degeneracy of the surface states. Applying a Zeeman field to the sample is predicted to shift the spin-polarized flat bands away from zero energy, thus splitting the zero-bias peak [24, 57, 107]. The absence of splitting for certain field orientations would strongly suggest nondegenerate bands, as doubly-degenerate bands are expected to be spin degenerate and split for any orientation of the applied field [108]. On the other hand, the stability of nodal NCSs in such Zeeman fields is uncertain [109, 110]. A less invasive variation on this approach is to replace the insulating tunneling barrier with a ferromagnetic insulator [85, 108].

The topological classification of nodal superconductors is only approximately valid in the presence of disorder. Even for a pristine bulk system, however, disorder at the surface or at the interface in a tunneling junction is inevitable. So long as the disorder is not too strong the conductance features discussed above remain detectable, although they are broadened by the finite lifetime of the quasiparticles [31, 111–114]. Extremely disordered surfaces produce 'dead' insulating layers, which redefine the edge of a superconductor [113–115]. This is illustrated in figures 9(a) and 9(b), which show the layer-resolved density of states of a $(d_{xy} + p)$-wave NCS [45] on a square lattice in the presence and absence of strong edge disorder, respectively. For very strong edge impurities, the states in the outermost layer are almost fully localized, while in the second and third inward layers new weakly disordered states reemerge.

5.2. Surface currents

A key signature of the chiral surface states of Weyl superconductors is that they show anomalous spin and thermal Hall conductance in the direction of their propagation [49, 116]. Although the zero-temperature Hall conductances are directly related to the Chern number, they also depend upon the number of chiral edge modes in the system, and so they are proportional to the separation of the Weyl points in momentum space. This is in contrast to the universal quantization in a fully-gapped time-reversal-symmetry breaking topological superconductor [117–119]. Furthermore, the spin Hall conductance in the triplet Weyl superconductor depends on the orientation of the magnetic field with respect to the **d**-vector, as not all spin directions are conserved [119]. While the measurement of the anomalous spin Hall conductance is likely to be very difficult [117], the anomalous thermal Hall conductance is predicted to be experimentally accessible for realistic materials [44, 120].

The chiral surface states may also carry a surface charge current, but it is not topologically protected since charge is not conserved in a superconductor. In particular, its detection is extremely difficult as it will be compensated for by Meissner screening currents [121]. While the current carried by the bound states is localized within a few coherence lengths ξ of the surface, however, the screening currents build up on the scale of the penetration depth λ, and so in extreme type-II superconductors a finite surface current density is expected. Precision magnetometry has so far failed to detect surface charge currents in Sr_2RuO_4 [122], despite otherwise compelling evidence that this is a chiral p-wave superconductor [123, 124]. The charge current is not universally related to the Chern number, however, and even ignoring the Meissner effect, it depends sensitively upon microscopic details of the superconductor [125, 126].

Surface currents might also arise in time-reversal invariant NCS. Ignoring SOC, the simplest model of a majority-triplet C_{4v} NCS is a superconducting analogue of the quantum spin Hall insulator [20], and the helical edge states therefore carry a surface spin current [86, 90, 127]. On the other hand, a surface spin current carried by states above the gap is present in the nontopological phase [89], and the spin current is strongly suppressed by the SOC [90]. Charge currents are also predicted to arise at the interface between NCSs and ferromagnets [83, 128, 129]. In particular, at surfaces with spin-polarized flat bands, the coupling to the exchange field of the ferromagnet generates a chiral electronic structure at the interface. The resulting charge current is very pronounced at low temperatures and shows nonanalytic dependence on the exchange field strength [83, 128].

5.3. Other proposals

There are a number of proposals for evidencing chiral or helical edge states based upon interference effects in the magnetoconductance of superconductor loops [130, 131], or nonlocal conductance at domain walls in Weyl superconductors [132]. Although such experiments could give unambiguous demonstration of the edge states, these proposals assume a fully-gapped pairing state, so it is unclear if they would apply to a nodal system.

The electromagnetic response of surface states may differ significantly from the bulk, which can be exploited as an experimental test of their existence. In particular, the flat bands at the (1 1 0) surface of the cuprate superconductors

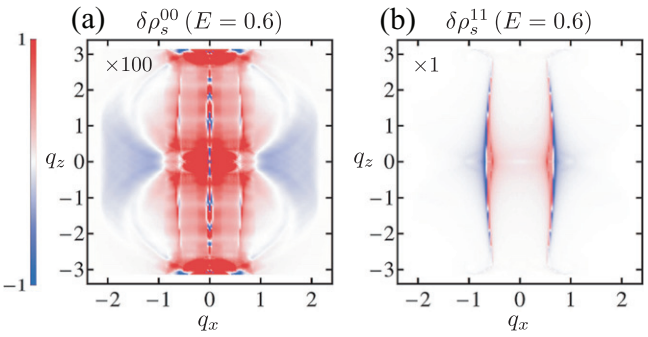

Figure 10. Fourier-transformed quasiparticle interference patterns for arc states at the (0 1 0) surface of a C_{4v} point group NCS. Results for (a) nonmagnetic scatterers and (b) magnetic scatterers with impurity moment along the x-axis. The weak and diffuse features in (a) reflect the suppression of backscattering due to the spin-polarization of the edge states. Backscattering occurs for magnetic scattering, giving rise to the much stronger and sharper features in (b). Figure adapted from [66].

show a paramagnetic response [133] to an applied magnetic field, which has been detected in tunneling [134] and penetration depth [135, 136] measurements. Although there is also a bulk contribution to this so-called nonlinear Meissner effect from the nodal quasiparticles [137], this has a very different temperature dependence compared to the surface state contribution [138], and recent experiments have been able to distinguish the two [139]. The nonlinear Meissner effect may therefore be a useful probe of the surface physics of other nodal topological superconductors.

The surface states of a topological superconductor could be more directly demonstrated using quasiparticle interference spectroscopy [66, 140], which has already been successfully used to evidence topological insulator surface states [141]. This can probe the spin character of the surface states, as scattering between states with opposite spin polarization (i.e. backscattering processes) are suppressed, unless the scattering is by magnetic impurities. Predictions [66] for NCS arc states are shown in figure 10: whereas nonmagnetic scattering gives a weak and diffuse signal (panel (a)), magnetic scattering produces a strong and well-defined image of the arc states (panel (b)).

6. Survey of candidate materials for nodal topological superconductivity

In certain materials with strong electronic correlations, topological superconductivity can occur naturally due to unconventional [142], i.e. non-phonon-mediated, pairing interactions. These unconventional pairing mechanisms (e.g. due to spin fluctuations) are in general quite anisotropic and hence give rise to nodal structures of the superconducting gap. As a consequence, topological superconductors with nodes are far more common than those with a full excitation gap. An important exception to this rule is the fully gapped spin-triplet superconductor Sr_2RuO_4 [123, 124]. In this section we give a brief overview of candidate materials for nodal topological superconductivity with either spin-triplet or spin-singlet pairing, which we list in tables 2 and 3, respectively.

We note that due to strong atomic SOC in many of these materials, the spin symmetry of the Cooper pairs is determined by the *pseudospins* of quasiparticles with opposite momenta, rather than by the real spins of electrons. Thus, the pairing symmetries may be better distinguished in terms of the parity of the orbital pair wavefunction. For simplicity, we nevertheless refer to odd- and even-parity states as spin triplet and singlet, respectively.

6.1. Nodal superconductors with spin-triplet pairing

A nodal spin-triplet pairing state has been established unambiguously in superfluid ^{3}He [52, 54]. That is, the A phase of ^{3}He is known to be described by the Anderson-Brinkman-Morel (ABM) state [53], a three-dimensional superfluid with nodal points at the north and south poles of the Fermi sphere. The ABM state is a member of symmetry class D with codimension $p = 3$ (see section 3.3.1). Hence, according to the classification of table 1, the point nodes of ^{3}He-A are topologically stable and protected by a two-dimensional Chern number [25–28].

Here, however, we want to focus on nodal topological *superconductors* rather than superfluids. A very promising group of materials for nodal topological superconductivity are the noncentrosymmetric superconductors (NCSs) [143, 144]. These systems have extremely diverse properties, however, as they are defined by their crystal structure as opposed to chemical composition. In particular, the parity-mixing of the gap depends upon microscopic details. The most interesting case for us is when the spin-triplet and spin-singlet components are comparable in magnitude, which generically leads to a nodal superconducting state as discussed in section 3. Sizable spin-triplet pairing components can be expected to occur in strongly correlated NCSs where the onsite Coulomb repulsion suppresses the spin-singlet s-wave channel, and where there are strong noncentrosymmetric spin fluctuations [145–147]. These conditions are believed to hold in the heavy fermion C_{4v} point group NCS $CePt_3Si$ [148], leading to an $(s + p)$-wave state [146]. Indeed, there is significant evidence of line nodes and an unconventional spin pairing state in this material [149–152]. A similar pairing state seems to be realized in $CeIrSi_3$ [153, 154] and $CeRhSi_3$ [155], which are also heavy fermion NCS with C_{4v} point group. Not all NCS with a sizable spin-triplet gap are so strongly correlated: Replacing Pd by Pt in the O point group NCS $Li_2(Pd_{1-x}Pt_x)B$ appears to tune the system from a conventional s-wave superconductor to a nodal triplet superconductor [156–158], but there is no evidence that the correlation strength is dramatically altered by this substitution. The gap structure of $LaNiC_2$ (C_{2v} point group) is controversial [159–161]. Muon spin rotation experiments evidence time-reversal-symmetry breaking in $LaNiC_2$ [159] and the related (centrosymmetric) $LaNiGa_2$ [162], suggesting nonunitary triplet pairing.

A number of Uranium-based heavy fermion compounds show strong evidence of unconventional triplet pairing states with nontrivial topological properties [175–178]. Among them, UPt_3 is probably the most promising candidate for

Table 2. List of candidate materials for nodal topological superconductivity with (majority) spin-triplet pairing. Note that in some materials the evidence is contradictory. NCS: Noncentrosymmetric superconductor. HF: Heavy fermion superconductor. FM: Ferromagnetic superconductor. NMR: Nuclear magnetic resonance. SH: Specific heat. UA: Ultrasound attenuation. TC: Thermal conductivity. PD: London penetration depth. H_{c2}: Upper critical field.

Material	Type	Evidence for triplet pairing	Evidence for nodes	Probable pairing symmetry
A phase of ^{3}He	Superfluid	NMR, magnetiz. [54]	SH [52]	chiral
$CePt_3Si$	NCS, HF	indirect	PD, NMR, etc [149–152]	$(s+p)$-wave
$CeIrSi_3$[a]	NCS, HF	NMR [153, 154]	NMR [153, 154]	$(s+p)$-wave
$CeRhSi_3$[a]	NCS, HF	H_{c2} [155]		?
Li_2Pt_3B	NCS	NMR [157]	PD, NMR, SH [156–158]	$(s+p)$-wave
$LaNiC_2$	NCS	Indirect [159]	PD [160]	Nonunitary
$LaNiGa_2$	Centro.	Indirect [162]		Nonunitary
URhGe	FM, HF	Indirect [163]	SH [164]	p-wave
UCoGe	FM, HF	NMR [165]	Indirect [166]	p-wave
UGe_2[a]	FM, HF	H_{c2} [167, 168]	NMR [169]	p-wave
UPt_3	HF	NMR [170]	SH, UA, TC [171]	Chiral f-wave
UBe_{13}	HF	NMR [172]	SH, NMR [173, 174]	Nodal

[a] Superconducting under pressure

spin-triplet superconductivity, and has received much attention [171]. This material has three different nodal superconducting phases, and there is strong evidence that one of these realizes a time-reversal-symmetry breaking chiral f-wave state, which is predicted to show Weyl nodes [120, 179]. The superconductivity of UBe_{13} is less well-understood, but evidence of surface states has been reported [180]. Intriguingly, some of these systems, in particular URhGe, UCoGe, and UGe_2, show an apparently cooperative coexistence of ferromagnetism and superconductivity [175, 178]. That is, close to a ferromagnetic quantum critical point ferromagnetic spin fluctuations mediate spin-triplet pairing. The natural pairing state for such systems would involve equal-spin-pairing $|\uparrow\uparrow\rangle$ and $|\downarrow\downarrow\rangle$ on the majority- and minority-spin Fermi surfaces, respectively. The crystal space group of most ferromagnetic superconductors is of low symmetry, which results in strong anisotropies of the magnetic fluctuations, favourable to the observed nodal pairing states. Topological properties of these systems are largely uninvestigated, although the existence of arc states connected with Weyl nodes has been proposed [140].

The relative rarity of intrinsic spin-triplet superconductors has led to a number of proposals to engineer such states in heterostructures involving spin-singlet superconductors [49, 50, 82, 181, 182]. A key to these proposals is the presence of strong SOC, which, under appropriate conditions, can accomplish a change in parity of the Cooper pairs, resulting in a sizable proximity-induced spin-triplet gap. For example, superlattices of topological insulators and s-wave superconductors are proposed to realize a p-wave Weyl superconductor [49, 50]. Incorporating high-temperature superconductors into such devices has the great advantage that the engineered spin-triplet superconductor could be realized at much higher temperatures than their intrinsic counterparts [82, 181, 182]. Particularly interesting is proximity-induced pairing in the surface states of a topological insulator [13, 181]. Recently, cuprate superconductor-topological insulator devices have been fabricated [183, 184]. However, the proximity-induced gap in these devices appears to be nodeless.

6.2. Nodal superconductors with spin-singlet pairing

High-temperature cuprate superconductors are probably the most extensively studied unconventional superconductors [142]. While there is no common consensus on the pairing mechanism, it is by now generally accepted that the pairing symmetry in the cuprates is of a $d_{x^2-y^2}$-wave form [35, 36]. That is, the superconducting gap changes sign along the Fermi surface, giving rise to four topologically protected point nodes. The superconducting state of the cuprates belongs to symmetry class CII in table 1, since it preserves both time-reversal and $SU(2)$ spin-rotation symmetry. Hence, it follows from the classification of table 1, that the point nodes are protected by a $2\mathbb{Z}$ topological number, i.e. by a winding number which takes on the values ± 2. Due to the bulk-boundary correspondence, the topological characteristics of these point nodes lead to the appearance of doubly degenerate (i.e. spin-degenerate) flat band edge states [33, 34]. These zero-energy edge modes have been observed in tunneling experiments on the cuprate material $YBa_2Cu_3O_{6-x}$ [94–96].

A superconducting gap with d-wave symmetry also occurs in the Cerium-based heavy fermion compounds $CeCu_2Si_2$ [191] and $CeXIn_5$, where X is a transition metal (Co, Ir, Rh) [37, 38]. In all these materials superconductivity appears close to an antiferromagnetic quantum critical point and is believed to be mediated by spin fluctuations [142, 177, 178]. In contrast to the ferromagnetic superconductors, however, magnetic order in the Cerium compounds competes with superconductivity. NMR measurements indicate spin-singlet pairing and in combination with specific heat and thermal conductivity measurements yield evidence for line nodes in the superconducting gap. Therefore, it seems likely that the order parameter symmetry in these heavy fermion superconductors is of a d-wave form.

Table 3. List of candidate materials for nodal topological superconductivity with (majority) spin-singlet pairing. HF: Heavy fermion superconductor. SL: Superlattice. ARPES: Angle-resolved photoemission spectroscopy. STM: Scanning tunneling microscopy. NMR: Nuclear magnetic resonance. PD: London penetration depth. SH: Specific heat. TC: Thermal conductivity. MT: Magnetic torque. PKE: Polar Kerr effect. μSR: Muon spin rotation.

Material	Type	Time-reversal symmetry	Evidence for nodes	Probable pairing symmetry
$YBa_2Cu_3O_{6+x}$, $La_{2-x}Sr_xCuO_4$, etc	High-temp. Supercond.	Yes	ARPES, STM, NMR, PD, etc [35, 36]	$d_{x^2-y^2}$-wave
$CeCu_2Si_2$	HF	Yes	Indirect [185]	d-wave
$CeCoIn_5$	HF	Yes	SH, TC, NMR, STM [37–40, 186]	$d_{x^2-y^2}$-wave
$CeIrIn_5$	HF	Yes	SH, TC, NMR [38, 186]	d-wave
$CeRhIn_5$ [a]	HF	Yes	SH [187]	d-wave
URu_2Si_2	HF	No (MT [43], PKE [188])	SH, NMR, TC [41, 42]	$(d \pm id)$-wave
SrPtAs	Pnictide	No (μSR [47])	Indirect [48]	$(d \pm id)$-wave
$CeCoIn_5/YbCoIn_5$	SL		Indirect [189]	Likely d-wave
$Cu_x(PbSe)_5(Bi_2Se_3)_6$	SL		SH [190]	line node

[a] Superconducting under pressure.

This has been confirmed for $CeCoIn_5$ by a careful analysis of the quasiparticle interference patterns observed in scanning tunneling spectroscopy [39, 40].

The table 3 lists two compounds which show signs of unconventional spin-singlet superconductivity with broken time-reversal symmetry. The first one is URu_2Si_2 [192], in which superconductivity emerges out of a somewhat mysterious 'hidden order phase'. Recently, a polar Kerr effect has been observed, which appears with the onset of superconductivity [188]. Together with specific heat [42] and thermal conductivity measurements [41], this suggests that URu_2Si_2 is a chiral d-wave superconductor, which breaks time-reversal symmetry. Such a state can support Weyl nodes [44]. The second candidate for time-reversal symmetry breaking superconductivity is the pnictide material SrPtAs. Muon spin-rotation measurements on SrPtAs have revealed time-reversal-symmetry breaking in the superconducting state [47]. This material is also predicted to realize a chiral d-wave state with Weyl nodes [48].

Artificial superconducting structures also hold much promise in realizing gapless topological singlet superconductors. Recently, superlattices of the $d_{x^2-y^2}$-wave superconductor $CeCoIn_5$ and the non-superconducting metal $YbCoIn_5$ have been grown, such that inversion symmetry is broken in the $CeCoIn_5$ layers [189]. This material is predicted to realize a nodal NCS with nondegenerate flat bands [45, 102]. Another intriguing compound is $Cu_x(PbSe)_5(Bi_2Se_3)_6$, where the doped topological insulator $Cu_xBi_2Se_3$ is combined with the topologically trivial insulator PbSe [190]. $Cu_xBi_2Se_3$ has attracted much attention as a candidate topological superconductor with a full (odd-parity) gap [193–195]. Surprisingly, specific heat measurements appear to indicate that the superconducting gap in $Cu_x(PbSe)_5(Bi_2Se_3)_6$ has line nodes. Note that we have conservatively classified the pairing as spin singlet, although the upper critical field hints at a more exotic gap symmetry. More speculatively, s-wave singlet superconductivity in doped Weyl semimetals is predicted to realize a Weyl superconductor [196], which may possess exotic crossed arc surface states [197].

7. Summary and outlook

In this review we have presented an introduction to the topological properties of nodal superconductors. Although the topology is less robust than in fully-gapped superconductors, nodal superconductors are more common than unconventional fully-gapped superconductors, and so this theory will likely find much application. In addressing this subject, we have introduced two important examples: time-reversal-symmetry-breaking Weyl superconductors (section 2.1), and time-reversal-invariant noncentrosymmetric superconductors (section 2.2), which can be regarded as prototypes of superconductors with topologically nontrivial point and line nodes, respectively.

At the heart of the review is section 3, and more specifically the topological classification of nodal superconductors summarized in table 1. We have organized our review around this classification scheme, since: (i) It brings order to the growing zoo of unconventional superconductors; (ii) it gives guidance for the search and design of new topological states; and (iii) it links the properties of the surface states to the bulk nodal structure and the symmetries of the order parameter. Point (iii) is particularly exciting, as it means that the pairing symmetry of an unconventional superconductor can be identified solely by means of surface measurements. Accurate modelling of the surface state spectrum is therefore an important aspect of the theory. This is discussed from the point of view of the popular quasiclassical approximation in section 4. While the theory agrees perfectly with the topological arguments, it also gives us access to physics beyond table 1, e.g. edge states without topological protection, and the physical attributes of all types of surface states. The latter is very useful input for designing experimental probes of the surface.

In section 6 we briefly surveyed a number of materials for which there is strong evidence of a nodal superconducting state with nontrivial topology. Demonstrating the existence of the topologically protected edge states, however, will be a significant experimental challenge. As we have discussed

in section 5, there have been many theoretical studies of the possible signatures of topological edge states, but only a few materials have been practically studied. While some systems are likely less suitable for such studies than others due to material-specific difficulties, the large number and diversity of candidate superconductors gives hope that direct detection of edge states is feasible. In this regards, proposals to realize a topological nodal superconducting state in heterostructures are very attractive, due to the fine experimental control over such systems. We expect this to be a major direction for both theoretical and experimental work. Another promising avenue for future research is to utilize the edge states of topological superconductors to design novel quantum devices, which might find technological applications in spin-eletronics and the development of new low-power electronics. A crucial first step towards the realization of such devices is the ability to control and manipulate the edge states using, for example, magnetic fields [83, 128, 181], electric fields [198, 199], or mechanical strain.

A significant omission in our discussion is the effect of interactions beyond their role in generating the superconducting gap. The BdG Hamiltonian, on which the topological classification is based, is a single-particle theory of the gapped state. Nevertheless, many candidate topological superconductors are strongly correlated materials, where interactions may exert a profound influence over the low temperature physics. The topological properties of interacting systems are of much interest, but remain poorly understood [200–203]. A complete classification of interacting systems in one dimension has been obtained using matrix product states [204–207], but such a classification is currently missing for higher dimensions. Although BdG theory generally gives a good description of unconventional superconductors (at least at a phenomenological level), interactions could still qualitatively alter the edge physics: For example, residual interactions may cause an instability of the surface states, in particular the flat bands with their divergent density of states. So far, attention has focused mainly on instabilities of the surface states of d-wave superconductors [111, 133, 208–210], although the instability of flat bands of spinless superconductors has also been studied [211].

To conclude, the discovery that electronic systems can have nontrivial topology has opened a new perspective on the fundamentals of condensed matter physics. Our review highlights the large changes wrought by this revolution in the subfield of nodal superconductivity, producing a new classification of this disparate class of materials by topological features of their gap structure. This does not supersede previous classifications, but rather complements them, and indeed it is already expected that workers in this field pay attention to topological properties. We can only see this trend continuing, and that it will not be long before consideration of topological aspects will become ubiquitous and unremarkable in the study of unconventional superconductivity.

Acknowledgments

We would like to thank our colleagues and collaborators A Akbari, Y Asano, C Ast, H Benia, P Biswas, B Bujnowski, K S Burch, P-Y Chang, W Chen, C-K Chiu, M Cuoco, S Das Sarma, I Eremin, M Fischer, J Goryo, P Goswami, I Gruzberg, J S Hofmann, P Horsch, K Kern, G Khaliullin, L Klam, D Lee, C-T Lin, A Ludwig, H Luetkens, D Manske, S Matsuura, W Metzner, C Mudry, T Neupert, Y Nohara, A Oleś, J P Paglione, D Peets, R Queiroz, S Rex, B Roy, S Ryu, J D Sau, M Sigrist, A Sudbø, Z Sun, R Thomale, C Timm, P Wahl, V M Yakovenko, and A Yaresko. Special thanks are due to Peter Horsch for his constructive comments on the manuscript. PMRB acknowledges support from Microsoft Station Q, LPS-CMTC, and JQI-NSF-PFC.

References

[1] Schnyder A P, Ryu S, Furusaki A and Ludwig A W W 2008 *Phys. Rev.* B **78** 195125
[2] Kitaev A 2009 *AIP Conf. Proc.* **1134** 22–30
[3] Schnyder A P, Ryu S, Furusaki A and Ludwig A W W 2009 *AIP Conf. Proc.* **1134** 10–21
[4] Ryu S, Schnyder A P, Furusaki A and Ludwig A W W 2010 *New J. Phys.* **12** 065010
[5] Hasan M Z and Kane C L 2010 *Rev. Mod. Phys.* **82** 3045–67
[6] Qi X L and Zhang S C 2011 *Rev. Mod. Phys.* **83** 1057–110
[7] Grinevich P and Volovik G 1988 *J. Low Temp. Phys.* **72** 371–80
[8] Salomaa M M and Volovik G E 1988 *Phys. Rev.* B **37** 9298–311
[9] Alicea J 2012 *Rep. Prog. Phys.* **75** 076501
[10] Beenakker C 2013 *Ann. Rev. Condens. Matter Phys.* **4** 113–36
[11] Nayak C, Simon S H, Stern A, Freedman M and Das Sarma S 2008 *Rev. Mod. Phys.* **80** 1083–159
[12] Stanescu T D and Tewari S 2013 *J. Phys.: Condens. Matter* **25** 233201
[13] Fu L and Kane C L 2008 *Phys. Rev. Lett.* **100** 096407
[14] Sau J D, Lutchyn R M, Tewari S and Das Sarma S 2010 *Phys. Rev. Lett.* **104** 040502
[15] Lutchyn R M, Sau J D and Das Sarma S 2010 *Phys. Rev. Lett.* **105** 077001
[16] Oreg Y, Refael G and von Oppen F 2010 *Phys. Rev. Lett.* **105** 177002
[17] Mourik V, Zuo K, Frolov S M, Plissard S R, Bakkers E P A M and Kouwenhoven L P 2012 *Science* **336** 1003–7
[18] Horava P 2005 *Phys. Rev. Lett.* **95** 016405
[19] Béri B 2010 *Phys. Rev.* B **81** 134515
[20] Sato M 2006 *Phys. Rev.* B **73** 214502
[21] Schnyder A P and Ryu S 2011 *Phys. Rev.* B **84** 060504
[22] Schnyder A P, Brydon P M R and Timm C 2012 *Phys. Rev.* B **85** 024522
[23] Brydon P M R, Schnyder A P and Timm C 2011 *Phys. Rev.* B **84** 020501
[24] Yada K, Sato M, Tanaka Y and Yokoyama T 2011 *Phys. Rev.* B **83** 064505
[25] Volovik G E 2003 *Universe in a Helium Droplet* (Oxford: Oxford University Press)
[26] Volovik G E 1992 *Exotic Properties of Superfluid* ^{3}*He* (*Series in Modern Condensed Matter Physics* vol 1) (Singapore: World Scientific)
[27] Volovik G E 2013 *Topology of Quantum Vacuum* (*Lecture Notes in Physics* vol 870) (Berlin: Springer)
[28] Volovik G E 2011 *JETP Lett.* **93** 66
[29] Heikkilä T, Kopnin N and Volovik G 2011 *JETP Lett.* **94** 233–9
[30] Heikkila T and Volovik G 2011 *JETP Lett.* **93** 59–65
[31] Dahlhaus J P, Gibertini M and Beenakker C W J 2012 *Phys. Rev.* B **86** 174520
[32] Kobayashi S, Shiozaki K, Tanaka Y and Sato M 2014 *Phys. Rev.* B **90** 024516

[33] Ryu S and Hatsugai Y 2002 *Phys. Rev. Lett.* **89** 077002
[34] Hu C R 1994 *Phys. Rev. Lett.* **72** 1526–9
[35] Scalapino D 1995 *Phys. Rep.* **250** 329–65
[36] Tsuei C C and Kirtley J R 2000 *Rev. Mod. Phys.* **72** 969–1016
[37] Izawa K, Yamaguchi H, Matsuda Y, Shishido H, Settai R and Onuki Y 2001 *Phys. Rev. Lett.* **87** 057002
[38] Movshovich R, Jaime M, Thompson J, Petrovic C, Fisk Z, Pagliuso P and Sarrao J 2001 *Phys. Rev. Lett.* **86** 5152–5
[39] Allan M P *et al* 2013 *Nat. Phys.* **9** 468–73
[40] Zhou B B *et al* 2013 *Nat. Phys.* **9** 474–9
[41] Kasahara Y, Iwasawa T, Shishido H, Shibauchi T, Behnia K, Haga Y, Matsuda T D, Onuki Y, Sigrist M and Matsuda Y 2007 *Phys. Rev. Lett.* **99** 116402
[42] Yano K, Sakakibara T, Tayama T, Yokoyama M, Amitsuka H, Homma Y, Miranović P, Ichioka M, Tsutsumi Y and Machida K 2008 *Phys. Rev. Lett.* **100** 017004
[43] Li G *et al* 2013 *Phys. Rev.* B **88** 134517
[44] Goswami P and Balicas L 2013 ArXiv e-prints (preprint 1312.3632)
[45] Tanaka Y, Mizuno Y, Yokoyama T, Yada K and Sato M 2010 *Phys. Rev. Lett.* **105** 097002
[46] Sato M, Tanaka Y, Yada K and Yokoyama T 2011 *Phys. Rev.* B **83** 224511
[47] Biswas P K *et al* 2013 *Phys. Rev.* B **87** 180503
[48] Fischer M H, Neupert T, Platt C, Schnyder A P, Hanke W, Goryo J, Thomale R and Sigrist M 2014 *Phys. Rev.* B **89** 020509
[49] Meng T and Balents L 2012 *Phys. Rev.* B **86** 054504
[50] Das T 2013 *Phys. Rev.* B **88** 035444
[51] Ohtomo A and Hwang H Y 2004 *Nature* **427** 423–6
[52] Vollhardt D and Wölfle P 2013 *The Superfluid Phases of Helium 3* (New York: Dover)
[53] Anderson P W and Morel P 1961 *Phys. Rev.* **123** 1911–34
[54] Wheatley J C 1975 *Rev. Mod. Phys.* **47** 415–70
[55] Möller G, Cooper N and Gurarie V 2011 *Phys. Rev.* B **83** 014513
[56] Frigeri P A, Agterberg D F, Koga A and Sigrist M 2004 *Phys. Rev. Lett.* **92** 097001
[57] Matsuura S, Chang P Y, Schnyder A P and Ryu S 2012 *New J. Phys.* **15** 065001
[58] Zhao Y X and Wang Z D 2013 *Phys. Rev. Lett.* **110** 240404
[59] Zhao Y X and Wang Z D 2014 *Phys. Rev.* B **89** 075111
[60] Shiozaki K and Sato M 2014 *Phys. Rev.* B **90** 165114
[61] Chiu C K and Schnyder A P 2014 *Phys. Rev.* B **90** 205136
[62] Zirnbauer M R 1996 *J. Math. Phys.* **37** 4986–5018
[63] Altland A and Zirnbauer M R 1997 *Phys. Rev.* B **55** 1142–61
[64] Essin A M and Gurarie V 2011 *Phys. Rev.* B **84** 125132
[65] Graf G and Porta M 2013 *Commun. Math. Phys.* **324** 851–95
[66] Hofmann J S, Queiroz R and Schnyder A P 2013 *Phys. Rev.* B **88** 134505
[67] Nakahara M 2003 *Geometry, Topology and Physics* (*Graduate Student Series in Physics*) 2nd edn (London: Taylor and Francis)
[68] Sato M, Tanaka Y, Yada K and Yokoyama T 2011 *Phys. Rev.* B **83** 224511
[69] Tanaka Y, Sato M and Nagaosa N 2012 *J. Phys. Soc. Japan* **81** 011013
[70] Sato M 2009 *Phys. Rev.* B **79** 214526
[71] Qi X L, Hughes T L and Zhang S C 2010 *Phys. Rev.* B **81** 134508
[72] Chiu C K and Schnyder A P 2015 ArXiv e-prints (preprint 1501.06820)
[73] Morimoto T and Furusaki A 2014 *Phys. Rev.* B **89** 235127
[74] Chang P Y, Matsuura S, Schnyder A P and Ryu S 2014 *Phys. Rev.* B **90** 174504
[75] Yang B J and Nagaosa N 2014 *Nat. Commun.* **5** 4898
[76] Tsutsumi Y, Ishikawa M, Kawakami T, Mizushima T, Sato M, Ichioka M and Machida K 2013 *J. Phys. Soc. Japan* **82** 113707
[77] Serene J W and Rainer D 1983 *Phys. Rep.* **101** 221
[78] Kashiwaya S and Tanaka Y 2000 *Rep. Prog. Phys.* **63** 1641
[79] Eschrig M 2000 *Phys. Rev.* B **61** 9061
[80] Eschrig M, Iniotakis C and Tanaka Y 2012 Properties of interfaces and surfaces in non-centrosymmetric superconductors *Non-Centrosymmetric Superconductors* ed E Bauer and M Sigrist (Berlin: Springer)
[81] Eilenberger G 1968 *Z. Phys.* **214** 195
[82] Takei S, Fregoso B M, Galitski V and Das Sarma S 2013 *Phys. Rev.* B **87** 014504
[83] Brydon P M R, Timm C and Schnyder A P 2013 *New J. Phys.* **15** 045019
[84] Schnyder A P, Brydon P M R, Manske D and Timm C 2010 *Phys. Rev.* B **82** 184508
[85] Brydon P M R, Schnyder A P and Timm C 2015 *New J. Phys.* **17** 013016
[86] Tanaka Y, Yokoyama T, Balatsky A V and Nagaosa N 2009 *Phys. Rev.* B **79** 060505
[87] Fujimoto S 2009 *Phys. Rev.* B **79** 220506
[88] Asano Y and Yamano S 2011 *Phys. Rev.* B **84** 064526
[89] Lu C K and Yip S 2010 *Phys. Rev.* B **82** 104501
[90] Vorontsov A B, Vekhter I and Eschrig M 2008 *Phys. Rev. Lett.* **101** 127003
[91] Iniotakis C, Hayashi N, Sawa Y, Yokoyama T, May U, Tanaka Y and Sigrist M 2007 *Phys. Rev.* B **76** 012501
[92] Rahnavard Y, Manske D and Annunziata G 2014 *Phys. Rev.* B **89** 214501
[93] Annunziata G, Manske D and Linder J 2012 *Phys. Rev.* B **86** 174514
[94] Kashiwaya S, Tanaka Y, Koyanagi M, Takashima H and Kajimura K 1995 *Phys. Rev.* B **51** 1350–3
[95] Alff L and *et al* 1997 *Phys. Rev.* B **55** R14757–60
[96] Wei J Y T, Yeh N C, Garrigus D F and Strasik M 1998 *Phys. Rev. Lett.* **81** 2542–5
[97] Kashiwaya S, Kashiwaya H, Kambara H, Furuta T, Yaguchi H, Tanaka Y and Maeno Y 2011 *Phys. Rev. Lett.* **107** 077003
[98] Tanaka Y and Kashiwaya S 1995 *Phys. Rev. Lett.* **74** 3451–4
[99] Deutscher G 2005 *Rev. Mod. Phys.* **77** 109–135
[100] Yamakage A, Yada K, Sato M and Tanaka Y 2012 *Phys. Rev.* B **85** 180509
[101] Yokoyama T, Tanaka Y and Inoue J 2005 *Phys. Rev.* B **72** 220504
[102] Yuan N F, Wong C L and Law K 2014 *Phys. E: Low-dimens. Syst. Nanostruct.* **55** 30–6
[103] Mukherjee S P 2011 *Eur. Phys. J.* B **80** 51–8
[104] Blonder G E, Tinkham M and Klapwijk T M 1982 *Phys. Rev.* B **25** 4515
[105] Daghero D and Gonnelli R S 2010 *Supercond. Sci. Technol.* **23** 043001
[106] Wu S and Samokhin K V 2009 *Phys. Rev.* B **80** 014516
[107] Wong C L M, Liu J, Law K T and Lee P A 2013 *Phys. Rev.* B **88** 060504
[108] Kashiwaya S, Tanaka Y, Yoshida N and Beasley M R 1999 *Phys. Rev.* B **60** 3572–80
[109] Eremin I and Annett J F 2006 *Phys. Rev.* B **74** 184524
[110] Loder F, Kampf A P and Kopp T 2013 *J. Phys.: Condens. Matter* **25** 362201
[111] Matsumoto M and Shiba H 1995 *J. Phys. Soc. Japan* **64** 1703–13
[112] Barash Y S, Svidzinsky A A and Burkhardt H 1997 *Phys. Rev.* B **55** 15282–94
[113] Queiroz R and Schnyder A P 2014 *Phys. Rev.* B **89** 054501
[114] Queiroz R and Schnyder A P 2015 *Phys. Rev.* B **91** 014202
[115] Schubert G, Fehske H, Fritz L and Vojta M 2012 *Phys. Rev.* B **85** 201105
[116] Volovik G E and Yakovenko V M 1989 *J. Phys.: Condens. Matter* **1** 5263

[117] Senthil T, Marston J B and Fisher M P A 1999 *Phys. Rev.* B **60** 4245–54
[118] Read N and Green D 2000 *Phys. Rev.* B **61** 10267–97
[119] Sengupta K, Roy R and Maiti M 2006 *Phys. Rev.* B **74** 094505
[120] Goswami P and Nevidomskyy A H 2014 ArXiv e-prints (preprint 1403.0924)
[121] Matsumoto M and Sigrist M 1999 *J. Phys. Soc. Japan* **68** 994–1007
[122] Kirtley J R, Kallin C, Hicks C W, Kim E A, Liu Y, Moler K A, Maeno Y and Nelson K D 2007 *Phys. Rev.* B **76** 014526
[123] Maeno Y, Kittaka S, Nomura T, Yonezawa S and Ishida K 2012 *J. Phys. Soc. Japan* **81** 011009
[124] Mackenzie A P and Maeno Y 2003 *Rev. Mod. Phys.* **75** 657–712
[125] Lederer S, Huang W, Taylor E, Raghu S and Kallin C 2014 *Phys. Rev.* B **90** 134521
[126] Huang W, Taylor E and Kallin C 2014 *Phys. Rev.* B **90** 224519
[127] Sato M and Fujimoto S 2009 *Phys. Rev.* B **79** 094504
[128] Schnyder A P, Timm C and Brydon P M R 2013 *Phys. Rev. Lett.* **111** 077001
[129] Ren C-D and Wang J 2013 *Eur. Phys. J.* B **86** 190
[130] Béri B 2012 *Phys. Rev.* B **85** 140501
[131] Diez M, Fulga I C, Pikulin D I, Wimmer M, Akhmerov A R and Beenakker C W J 2013 *Phys. Rev.* B **87** 125406
[132] Serban I, Béri B, Akhmerov A R and Beenakker C W J 2010 *Phys. Rev. Lett.* **104** 147001
[133] Fogelström M, Rainer D and Sauls J A 1997 *Phys. Rev. Lett.* **79** 281–4
[134] Aprili M, Badica E and Greene L H 1999 *Phys. Rev. Lett.* **83** 4630–3
[135] Walter H, Prusseit W, Semerad R, Kinder H, Assmann W, Huber H, Burkhardt H, Rainer D and Sauls J A 1998 *Phys. Rev. Lett.* **80** 3598–601
[136] Carrington A, Manzano F, Prozorov R, Giannetta R W, Kameda N and Tamegai T 2001 *Phys. Rev. Lett.* **86** 1074–7
[137] Yip S K and Sauls J A 1992 *Phys. Rev. Lett.* **69** 2264–7
[138] Zare A, Dahm T and Schopohl N 2010 *Phys. Rev. Lett.* **104** 237001
[139] Zhuravel A P, Ghamsari B G, Kurter C, Jung P, Remillard S, Abrahams J, Lukashenko A V, Ustinov A V and Anlage S M 2013 *Phys. Rev. Lett.* **110** 087002
[140] Sau J D and Tewari S 2012 *Phys. Rev.* B **86** 104509
[141] Roushan P, Seo J, Parker C V, Hor Y S, Hsieh D, Qian D, Richardella A, Hasan M Z, Cava R J and Yazdani A 2009 *Nature* **460** 1106–9
[142] Norman M R 2014 Unconventional superconductivity *Novel Superfluids* vol 2, ed K H Bennemann and J B Ketterson (Oxford: Oxford University Press)
[143] Bauer E and Sigrist M 2012 *Non-Centrosymmetric Superconductors: Introduction and Overview* (*Lecture Notes in Physics* vol 847) (Berlin: Springer)
[144] Yip S 2014 *Ann. Rev. Condens. Matter Phys.* **5** 15
[145] Yokoyama T, Onari S and Tanaka Y 2007 *Phys. Rev.* B **75** 172511
[146] Yanase Y and Sigrist M 2008 *J. Phys. Soc. Japan* **77** 124711
[147] Takimoto T and Thalmeier P 2009 *J. Phys. Soc. Japan* **78** 103703
[148] Bauer E, Hilscher G, Michor H, Paul C, Scheidt E W, Gribanov A, Seropegin Y, Noël H, Sigrist M and Rogl P 2004 *Phys. Rev. Lett.* **92** 027003
[149] Bonalde I, Brämer-Escamilla W and Bauer E 2005 *Phys. Rev. Lett.* **94** 207002
[150] Izawa K, Kasahara Y, Matsuda Y, Behnia K, Yasuda T, Settai R and Onuki Y 2005 *Phys. Rev. Lett.* **94** 197002
[151] Mukuda H *et al* 2009 *J. Phys. Soc. Japan* **78** 014705
[152] Takeuchi T, Yasuda T, Tsujino M, Shishido H, Settai R, Harima H and Onuki Y 2007 *J. Phys. Soc. Japan* **76** 014702
[153] Mukuda H, Fujii T, Ohara T, Harada A, Yashima M, Kitaoka Y, Okuda Y, Settai R and Onuki Y 2008 *Phys. Rev. Lett.* **100** 107003
[154] Mukuda H, Ohara T, Yashima M, Kitaoka Y, Settai R, Onuki Y, Itoh K M and Haller E E 2010 *Phys. Rev. Lett.* **104** 017002
[155] Kimura N, Ito K, Aoki H, Uji S and Terashima T 2007 *Phys. Rev. Lett.* **98** 197001
[156] Yuan H Q, Agterberg D F, Hayashi N, Badica P, Vandervelde D, Togano K, Sigrist M and Salamon M B 2006 *Phys. Rev. Lett.* **97** 017006
[157] Nishiyama M, Inada Y and Zheng G q 2007 *Phys. Rev. Lett.* **98** 047002
[158] Eguchi G, Peets D C, Kriener M, Yonezawa S, Bao G, Harada S, Inada Y, Zheng G q and Maeno Y 2013 *Phys. Rev.* B **87** 161203
[159] Hillier A D, Quintanilla J and Cywinski R 2009 *Phys. Rev. Lett.* **102** 117007
[160] Bonalde I, Ribeiro R L, Syu K J, Sung H H and Lee W H 2011 *New J. Phys.* **13** 123022
[161] Chen J, Jiao L, Zhang J L, Chen Y, Yang L, Nicklas M, Steglich F and Yuan H Q 2013 *New J. Phys.* **15** 053005
[162] Hillier A D, Quintanilla J, Mazidian B, Annett J F and Cywinski R 2012 *Phys. Rev. Lett.* **109** 097001
[163] Hardy F and Huxley A D 2005 *Phys. Rev. Lett.* **94** 247006
[164] Aoki D *et al* 2001 *Nature* **413** 613
[165] Hattori T, Ihara Y, Karube K, Sugimoto D, Ishida K, Deguchi K, Sato N K and Yamamura T 2014 *J. Phys. Soc. Japan* **83** 061012
[166] Huy N T, de Nijs D E, Huang Y K and de Visser A 2008 *Phys. Rev. Lett.* **100** 077002
[167] Saxena S S *et al* 2000 *Nature* **406** 587–92
[168] Sheikin I, Huxley A, Braithwaite D, Brison J P, Watanabe S, Miyake K and Flouquet J 2001 *Phys. Rev.* B **64** 220503
[169] Harada A, Kawasaki S, Mukuda H, Kitaoka Y, Haga Y, Yamamoto E, Onuki Y, Itoh K M, Haller E E and Harima H 2007 *Phys. Rev.* B **75** 140502
[170] Tou H, Kitaoka Y, Ishida K, Asayama K, Kimura N, Onuki Y, Yamamoto E, Haga Y and Maezawa K 1998 *Phys. Rev. Lett.* **80** 3129–32
[171] Joynt R and Taillefer L 2002 *Rev. Mod. Phys.* **74** 235–94
[172] Tou H, Tsugawa N, Sera M, Haga Y and Onuki Y 2007 *J. Magn. Magn. Mater.* **310** 706–8 (*Proc. of the 17th Int. Conf. on Magnetism*)
[173] Ott H R, Rudigier H, Rice T M, Ueda K, Fisk Z and Smith J L 1984 *Phys. Rev. Lett.* **52** 1915–8
[174] MacLaughlin D E, Tien C, Clark W G, Lan M D, Fisk Z, Smith J L and Ott H R 1984 *Phys. Rev. Lett.* **53** 1833–6
[175] Flouquet J *et al* 2003 *Acta Phys. Pol.* B **34** 275
[176] Brison J P, Glémot L, Suderow H, Huxley A, Kambe S and Flouquet J 2000 *Phys. B: Condens. Matter* **280** 165–71
[177] Riseborough P, Schmiedeshoff G and Smith J 2008 *Springer Series in Solid State Sciences* (Berlin: Springer)
[178] Pfleiderer C 2009 *Rev. Mod. Phys.* **81** 1551–624
[179] Strand J D, Van Harlingen D J, Kycia J B and Halperin W P 2009 *Phys. Rev. Lett.* **103** 197002
[180] Wälti C, Ott H R, Fisk Z and Smith J L 2000 *Phys. Rev. Lett.* **84** 5616–9
[181] Linder J, Tanaka Y, Yokoyama T, Sudbø A and Nagaosa N 2010 *Phys. Rev. Lett.* **104** 067001
[182] Zhang F, Kane C L and Mele E J 2013 *Phys. Rev. Lett.* **111** 056402
[183] Zareapour P *et al* 2012 *Nat. Commun.* **3** 1056
[184] Wang E *et al* 2013 *Nat. Phys.* **9** 621
[185] Vieyra H A, Oeschler N, Seiro S, Jeevan H S, Geibel C, Parker D and Steglich F 2011 *Phys. Rev. Lett.* **106** 207001

[186] Kohori Y, Yamato Y, Iwamoto Y, Kohara T, Bauer E, Maple M and Sarrao J 2001 *Phys. Rev.* B **64** 134526
[187] Fisher R A *et al* 2002 *Phys. Rev.* B **65** 224509
[188] Schemm E R, Baumbach R E, Tobash P H, Ronning F, Bauer E D and Kapitulnik A 2015 *Phys. Rev.* B **91** 140506(R)
[189] Shimozawa M *et al* 2014 *Phys. Rev. Lett.* **112** 156404
[190] Sasaki S, Segawa K and Ando Y 2014 *Phys. Rev.* B **90** 220504
[191] Steglich F, Aarts J, Bredl C, Lieke W, Meschede D, Franz W and Schäfer H 1979 *Phys. Rev. Lett.* **43** 1892–6
[192] Mydosh J and Oppeneer P 2011 *Rev. Mod. Phys.* **83** 1301–22
[193] Fu L and Berg E 2010 *Phys. Rev. Lett.* **105** 097001
[194] Kriener M, Segawa K, Ren Z, Sasaki S and Ando Y 2011 *Phys. Rev. Lett.* **106** 127004
[195] Levy N, Zhang T, Ha J, Sharifi F, Talin A A, Kuk Y and Stroscio J A 2013 *Phys. Rev. Lett.* **110** 117001
[196] Cho G Y, Bardarson J H, Lu Y M and Moore J E 2012 *Phys. Rev.* B **86** 214514
[197] Lu B, Yada K, Sato M and Tanaka Y 2015 *Phys. Rev. Lett.* **114** 096804
[198] Ezawa M 2015 *Phys. Rev. Lett.* **114** 056403
[199] Wray L A, Xu S, Neupane M, Fedorov A V, Hor Y S, Cava R J and Hasan M Z 2013 *J. Phys.: Conf. Ser.* **449** 012037
[200] Fidkowski L and Kitaev A 2010 *Phys. Rev.* B **81** 134509
[201] Fidkowski L, Chen X and Vishwanath A 2013 *Phys. Rev.* X **3** 041016
[202] Wang C and Senthil T 2014 *Phys. Rev.* B **89** 195124
[203] Gu Z C and Wen X G 2014 *Phys. Rev.* B **90** 115141
[204] Pollmann F, Turner A M, Berg E and Oshikawa M 2010 *Phys. Rev.* B **81** 064439
[205] Chen X, Gu Z C and Wen X G 2011 *Phys. Rev.* B **83** 035107
[206] Schuch N, Pérez-Garcia D and Cirac I 2011 *Phys. Rev.* B **84** 165139
[207] Pollmann F, Berg E, Turner A M and Oshikawa M 2012 *Phys. Rev.* B **85** 075125
[208] Covington M, Aprili M, Paraoanu E, Greene L H, Xu F, Zhu J and Mirkin C A 1997 *Phys. Rev. Lett.* **79** 277–80
[209] Honerkamp C, Wakabayashi K and Sigrist M 2000 *Europhys. Lett.* **50** 368
[210] Potter A C and Lee P A 2014 *Phys. Rev. Lett.* **112** 117002
[211] Li Y, Wang D and Wu C 2013 *New J. Phys.* **15** 085002